Final Report

Mathematical Modeling of Heat Transfer Enhancement by Coupling between Electrohydrodynamics and Extended Surface Techniques

Asst. Prof. Dr. Nat Kasayapanand (King Mongkut's University of Technology Thonburi)

Prof. Dr. Tanongkiat Kiatsiriroat (Chiang Mai University)

September 2008

Final Report

Mathematical Modeling of Heat Transfer Enhancement by Coupling between Electrohydrodynamics and Extended Surface Techniques

Asst. Prof. Dr. Nat Kasayapanand (King Mongkut's University of Technology Thonburi)

Prof. Dr. Tanongkiat Kiatsiriroat (Chiang Mai University)

Supported by Commission on Higher Education and the Thailand Research Fund

ABSTRACT

Mathematical modeling of the electric field effect on natural and forced convections is investigated. The interactions between electric, flow, and temperature fields are analyzed by a computational fluid dynamics technique. Flow and temperature fields are substantially affected by the supplied voltage especially at low primary fluid velocity. The characteristics of flow and heat transfer enhancements are considered incorporating with the function of supplied voltage, fluid velocity, heat flux, electrode arrangement, and number of electrodes. Optimized relation between the number of fins and fin length is also obtained.

Keywords: Computational fluid dynamics; Mathematical modeling; Electrohydrodynamic; Electric field; Heat transfer enhancement

บทคัดย่อ

งานวิจัยนี้เป็นการสร้างแบบจำลองทางคณิตศาสตร์ของผลเนื่องจากสนามไฟฟ้าที่มีต่อการพาความร้อนแบบธรรมชาติและแบบบังคับ ความสัมพันธ์ระหว่างสนามไฟฟ้า สนามการไหล และสนามอุณหภูมิถูกวิเคราะห์โดยวิธีการคำนวณพลศาสตร์ของไหล ผลที่ได้พบว่ารูปแบบการไหลและความหนาของชั้นขอบเขตความร้อนถูกรบกวนเนื่องจากผลของสนามไฟฟ้า การเพิ่มความสามารถในการถ่ายเทความร้อนมีความสัมพันธ์กับแรงดันไฟฟ้าที่อิเลคโทรดและมีค่าสูงเมื่อความเร็วเริ่มต้นของของไหลมีค่าน้อย ผลที่ได้พบว่าลักษณะของการไหลและการเพิ่มความสามารถในการถ่ายเทความร้อนขึ้นอยู่กับ ขนาดแรงดันไฟฟ้า ความเร็วและทิศทางการไหล ปริมาณความร้อนที่ถ่ายเท การจัดวางอิเลคโทรดและจำนวนอิเลคโทรด รูปร่าง จำนวน และการจัดวางครีบ เงื่อนไขที่ขอบของครีบ

คำสำคัญ: การคำนวณพลศาสตร์ของไหล; แบบจำลองทางคณิตศาสตร์; สนามไฟฟ้า; การเพิ่มความสามารถในการถ่ายเทความร้อน

EXECUTIVE SUMMARY

Objectives

- To determine the flow patterns and the temperature distributions of air flowing through the extended surfaces under an electric field.
- Analyze the effect of all concerning parameters to the heat transfer coefficient such as the supplied voltage at wire electrode, Reynolds number, electrode arrangement, distance between wire electrodes, geometry and dimension of the extended surface, etc.
- To find out the optimized condition of the combination between electrohydrodynamics and extended surfaces techniques.

Research Methodology

- Study theory and literature review.
- Generate mathematical modeling of combination between electric field, flow field, and temperature field.
- Create computer programming for calculating air velocity profiles and temperature distributions through the fin under electric field by coupling between electrohydrodynamics and extended surface techniques.
- Analyze the effect of all parameters to the heat transfer coefficient comprising; size, shape, number, arrangement of fin, fluid velocity and direction, supplied voltage, electrode arrangement, distance between grounded surface and electrode, distance between electrodes, number of electrodes per length.

Conclusions

- Flow pattern of the fluid is affected by the supplied voltage. The thermal boundary layer along the surface is perturbed by the electric field effect and also decreases at high supplied voltage.
- The enhancement of heat transfer coefficient with the presence of an electric field increases in relation with the higher supplied voltage but decreases when the Reynolds number and Rayleigh number is augmented.

- Channel height affects to the collector efficiency. Lower the height gives stronger strength of the electric field which results in better thermal performance.
- The heat transfer also depends on the electrode arrangement, number of electrodes, and grounded surface geometry.
- For open channel and open cavity, the volume flow rate enhancement reaches to a maximum at an intermediate number of electrodes and reduces furthermore when the number of electrodes is rather high due to the pressure drop effect.
- The best augmented heat transfer for a fixed number of electrodes yields a recommended ratio of unity for the distance between wire electrodes to the distance between the grounded plates.
- For optimum design of finned configuration, it should be considering the constraint between all concerning parameters.

Output

1. Kasayapanand N, Kiatsiriroat T. *Enhanced heat transfer in partially open square cavities with thin fin by using electric field.* Energy Conversion and Management (accepted).
2. Kasayapanand N. *A computational fluid dynamics modeling of natural convection in finned enclosure under electric field.* Applied Thermal Engineering (in press).
3. Kasayapanand N. *Electrohydrodynamic enhancement of heat transfer in vertical fin array using computational fluid dynamics technique*. International Communications in Heat and Mass Transfer **2008**; 35: 762-770.
4. Kasayapanand N. *Enhanced heat transfer in inclined solar chimneys by electrohydrodynamic technique*. Renewable Energy **2008**; 33: 444-453.
5. Kasayapanand N. *Numerical modeling of the effect of number of electrodes on natural convection in an EHD fluid.* Journal of Electrostatics **2007**; 65: 465-474.
6. Kasayapanand N. *Numerical modeling of natural convection in partially open square cavities under electric field.* International Communications in Heat and Mass Transfer **2007**; 34: 630-643.
7. Kasayapanand N. *Electrode arrangement effect on natural convection*. Energy Conversion and Management **2007**; 48: 1323-1330.

8. Kasayapanand N, Kiatsiriroat T. *Numerical modeling of the electrohydrodynamic effect to natural convection in vertical channels*. International Communications in Heat and Mass Transfer **2007**; 34: 162-175.
9. Kasayapanand N, Kiatsiriroat T. *Optimized mass flux ratio of double-flow solar air heater with EHD*. Energy **2007**; 32: 1343-1351.

ACKNOWLEDGEMENTS

The author acknowledges with gratitude his indebtedness to Prof. Dr. Tanongkiat Kiatsiriroat who has made helpful suggestions for this research. The author gratefully acknowledges the financial support provided from the Commission on Higher Education and Thailand Research Fund in carrying out this study.

The author wishes to give the special thanks to his grandmother, parents, and family for their love and support.

CONTENTS

Page

NOMENCLATURE

Symbol		Unit
AR	aperture size (a/H)	
AH	aperture position (b/H)	
c_p	specific heat	J/kg·K
D	diameter	m
D_e	charge diffusion coefficient	$m^2/V·s$
D_p	charged particle diffusion coefficient	m^2/s
$\boldsymbol{E}$	electric field strength	V/m
$\boldsymbol{f}_D$	aerodynamic drag force	N/m^3
f_u	under relaxation factor	
$\boldsymbol{F}_E$	electrohydrodynamic body force	N/m^3
$\boldsymbol{g}$	acceleration due to gravity	m/s^2
Gr	Grashof number	
h	heat transfer coefficient	$W/m^2·K$
H	height	m
$\boldsymbol{J}$	current density	A/m^2
k	thermal conductivity	W/m·K
l_w	length between wire electrodes	m
L	channel length	m
m	total mass flux	kg/s
n	normal direction to the surface	
N_e	number of electrodes	
N_f	number of fins	
Nu	Nusselt number	
P	pressure	N/m^2
Pe	Peclet number	
Pr	Prandtl number	
q	electric charge density	C/m^3
q_h	heat flux	W/m^2
Q	heat transfer rate	W

r	corona wire radius	m
Ra	Rayleigh number	
Re	Reynolds number	
S	source term in ion continuity equation	$C/m^3 \cdot s$
t	time	s
T	temperature	K
$\boldsymbol{u}_e$	electric characteristic velocity	m/s
U_i	inlet air velocity	m/s
$\boldsymbol{v}$	fluid velocity	m/s
V	voltage	V
x	Cartesian coordinates	m
y	Cartesian coordinates	m
W	width	m

Greek symbols

α	thermal diffusivity	m^2/s
β	volume expansion coefficient	1/K
ε	fluid permittivity	F/m
γ	ratio of electric current	
η	curvilinear coordinate	m
λ	wave length	m
μ	dynamic viscosity	kg/m·s
μ_t	turbulent viscosity	kg/m·s
ϕ	inclined angle	degree
ν	kinematics viscosity	m^2/s
θ	dimensionless temperature	
ρ	density	kg/m^3
σ_e	electrical conductivity	1/ohm·m
τ	period	
ω	relaxation factor	
$\boldsymbol{\omega}$	vorticity	1/s
ξ	curvilinear coordinate	m

ψ	stream function	m^2/s

Subscripts

0	without electric field
a	ambient
EHD	based on electrical velocity
g	glass
i	indical notation of tensor
k	indical notation of tensor
L	lower subchannel
U	upper subchannel
new	updated value
m	mean value
p	charged particles
P	at the grounded plate
t	turbulent
w	wall surface

Superscripts

n	iteration number
∗	adjusted value

CHAPTER 1 INTRODUCTION

1.1 State of Problems and Background

The rate of energy consumption is continuously growing every year. The alternative energy especially free energy plays much important role in many countries. Solar air heaters are the key elements in many applications and it has been extensively investigated during the past three decades in an effort to develop more economical and efficient unit. The solar air heater occupies an important place among solar heating systems because of its several advantages, such as, minimal use of materials, phase change of the fluid does not occur, operating at low fluid pressure, neglecting corrosion and maintenance problems, etc. However, solar air heater is limited in its thermal performance due to the low density, the small volumetric heat capacity and the small heat conductivity of air. The strategies to achieve considerable heat transfer improvement are to use extended area by attaching fins, modify flow patterns, or increase fluid velocity. With these techniques, higher pressure drop of fluid flow is obtained. The enhancement technique utilizing electric field, which is based on electrostatic force due to space charge or polarization of dielectric fluid, can be one of the most promising methods among various active techniques because of its several advantages. For example, quick responses to control the flow, significant increase in heat transfer rate with very low pressure drop, and small consumption of electric power.

This research work investigates numerically the electrohydrodynamic (EHD) heat transfer enhancement using computational fluid dynamics (CFD) techniques for laminar forced convection of air flowing in solar collector and the results will be verified with experimental work. The electric field in the channel is generated by DC high voltage through the wire electrodes. The finite difference analysis is conducted by taking account of the interactions among electric field, flow field, and temperature field. The effect of all parameters such as supplied voltage at the wire electrode, Reynolds number, electrode arrangement, number of electrodes, absorber geometry, flow arrangement, geometry and dimensions of solar air heater, etc. are considered.

1.2 Objectives

1.2.1 To determine the flow patterns and the temperature distributions of air flowing inside solar air heater under electric field.

1.2.2 Analyze the effect of the parameters to the heat transfer coefficient comprising of supplied voltage at the wire electrode, Reynolds number, electrode arrangement, number of electrodes, absorber geometry, flow arrangement, geometry and dimension of solar air heater.

1.2.3 To find out an optimum design of electrohydrodynamic solar air heater.

1.3 Scopes

1.3.1 This research consider only single pass flat-plate solar air heater.

1.3.2 The fluid is single phase flow and the physical properties are assumed to be constant.

1.3.3 Flow characteristics are laminar, incompressible, and viscous.

1.3.4 The corona discharge occurs only in the vicinity around the wire electrode.

1.3.5 The effect of magnetic field is negligible.

1.4 Expected Benefit

1.4.1 The obtained results can be applied to design electrohydrodynamic solar air heater.

1.4.2 Create the theoretical modeling for developing in the future applications.

CHAPTER 2 LITERATURE REVIEW

The solar air heater occupies an important place among solar heating systems because of its several advantages such as minimal use of materials, phase change of the fluid does not occur, operating at low fluid pressure, neglecting corrosion and maintenance problems, etc. A flat plate solar air heater, in its simplest form, consists of one or more sheets of glass or transparent material situated above an absorbing plate with the air flowing either over or under the absorbing plate (Whillier [1], Close [2], Whillier [3], Gupta and Garg [4], Tan and Charters [5], Close and Dunkle [6], Liu and Sparrow [7], and Parkar [8]). One way to achieve considerable improvement in collector efficiency is to use an extended heat-transfer area (Yeh and Ting [9]) by attaching fins to a flat-plate type of solar air heater. Recently, several investigators designed two-pass operations with internal or external reflux at the other end. Satcunanathan and Deonarine [10] constructed a two-pass air heater in which the air flows through the glass panes before passing through the blackened metal collector. Wijeysundera et al. [11] developed two-pass flow arrangements, and the design curves for those devices over a range of variables were also presented. They considered the steady state heat balance equations which linked heater efficiency and heat removal factors with airflow rates, heat transfer coefficients between air streams and channel surfaces for various configurations. Garg et al. [12] also developed the theory of multiple pass solar air heaters.

The analysis of heat transfer in the channel has been performed under different boundary and operating conditions. Therefore, the heat transfer is being considered as mixed or combined between free and forced convections, especially, under laminar flow conditions with high temperature gradients and low velocity values. The instability caused by the buoyancy force acting to the fluid creates secondary flow conditions resulting in a significant increase in tile heat transfer rate. At the same time, the thermal entry length is reduced and early transition to turbulence is promoted. A classification of natural, forced, and mixed convection regimes were made by Metais and Eckert [13]. Initial investigations of mixed convection heat transfer were made on horizontal and inclined plates. Later studies were extended to parallel plates and then to the flow in channels. The study of forced convective heat transfer by Mori and Uchida [14] was being regarded as one of the first studies made on horizontal flat plates. From their theoretical and experimental

investigations, they concluded that for sufficiently high temperature differences between the plates the flow became three-dimensional caused by vortex rolls. It was also found that these vortex rolls increased the Nusselt number. Buoyancy effects were included by Cheng et al. [15] in a numerical study of laminar forced convection in horizontal rectangular channels. They reported that the buoyancy effect was negligible up to a certain entry length depending on the magnitude of the Rayleigh number. The longitudinal variation of the Nusselt number was characterized by a decaying oscillation (Incropera et al. [16] and Maughan and Incropera [17]). Moreover, increasing the aspect ratio increased both the entrance length and the Nusselt number. Experiments were performed by Osborne and lncropera [18] in order to determine the effects of free convection on laminar forced convection flow between horizontal parallel plates under symmetrical and asymmetrical heating conditions. Their experimental measurements showed that the flow at the top was characterized by laminar forced convection; however, conditions at the bottom plate were strongly influenced by buoyancy-induced flow. As a result of this buoyancy driven flow, mixed convection coefficients exceeded those associated with pure forced convection by as much as a factor of seven. Although buoyancy effects could significantly enhance heat transfer for laminar forced convection flows, enhancement was typically negligible if the forced flow is turbulent (Osborn and Incropera [19]). Lund [20] used a two-dimensional model for the transfer of heat in flat plate solar collector absorbers with adiabatic boundary conditions at the upper and lower edges of the collector. He solved approximately the governing partial differential equations analytically in terms of perturbation series. In similarity to heat exchanger theory, collector performance was stated in terms of absorber thermal effectiveness and number of transfer unit relationship.

There are some earlier studies relating to the effect of the ionic wind in electrostatic field, for instances, Yabe et al. [21] conducted an experiment on a corona wind between wire and plate electrodes. The report of Velkoff and Godfrey [22] on the heat transfer over a horizontal flat plate with parallel wire electrodes suggested that the ionic wind promoted the mixing of the primary flow resulting to the increases of heat transfer coefficient and this phenomenal characteristic was confirmed again by Yamamoto and Velkoff [23]. Franke and Hogue [24] studied heat transfer from horizontal tube with the corona discharge. Kikuchi et al. [25] proposed an analysis of the governing equations in electric, flow, and temperature fields to solve the thermal boundary layer equation under constant heat flux condition by profile method. Lean and Domoto [26] investigated the model of the physical of charge transport in steady Navier-Stroke's flow by using a novel algorithm that

considered full coupling of the electrostatic and fluid equations and was applicable to arbitrary geometries. In a forced convection field, the EHD induced flow takes place owing to the interaction between the ionic wind and the primary flow increases the convective heat transfer coefficient from the wall surface. Several models have been proposed for the calculation of the electric field and charge density distribution in a wire-plate precipitation system using the finite difference method (McDonald et al. [27] and Lawless and Sparks [28]). The main drawback of the finite difference method is the difficulty in the construction of the computational grid, which should be orthogonal to avoid complexity of the equations, and also must be significantly finer than the wire radius to produce grid-independent results, especially near the wire (Kallio and Stock [29]). In case of Cartesian grids, this can be accomplished either by the use of a fine mesh throughout the space, consuming thus excessive computer time, or by implementing numerical techniques for multi-blocks of variable grid density or local grid refinement around the wire. Such techniques can reduce the computer time demands, but the problem of matching the Cartesian grid lines and the circular surface of the wire remains. On the other hand, orthogonal curvilinear grids require special algorithms to construct, but they can be fitted to all the field space boundaries and easily achieve the desired resolution near the wire with considerably less total number of nodes.

The recently literatures can be grouped in the experimental works and the theoretical works. The details of distinct literatures are described as the followings;

2.1 Experimental Researches

Yabe [30] proposed the characteristics of active heat transfer enhancement technique by applying electric field. Also described were the EHD body force, corresponding governing equations and boundary conditions of EHD phenomena, as well as the relaxation time of an electric charge as shown in Fig. 2.1. Furthermore, the present state of research on EHD heat transfer enhancement techniques was systematically described from the EHD viewpoint. It was found that the convective heat transfer coefficients (with an EHD liquid jet) were enhanced by a factor of over 100 compared to the natural convection heat transfer coefficients. Maximum heat transfer coefficients, exceeding 10^4 W/m^{2}K, were related to not only by the forced convection of EHD liquid jet but also by the turbulent heat flux due to its turbulent intensity.

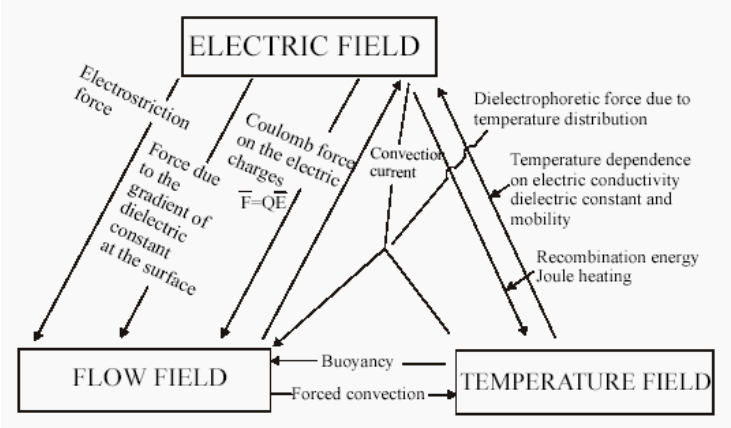

Fig. 2.1 Interactions among electric field, flow field, and temperature field [30].

Ishiguro [31] studied the augmentation effect of EHD induced flow disturbance on forced convection heat transfer in a channel. The applicability of the enhanced heat transfer was determined in a low pressure drop heat exchanger, such as high performance oil cooler. The investigation was mainly based on the study carried out on the unique point where the flow was disturbed actively and controllably by applying electric field between the wall and array of wire electrodes installed near the wall along the main stream. The liquid mixture of R-113 and ethanol was selected in the turbulent flow as well as in the laminar flow, up to a factor of about twenty-three in the case of laminar flow. It was noted that the rate of increase in heat transfer coefficient is larger compared to that in the pressure drop. From a measurement of velocities by a laser Doppler velocimeter, it was made clear that the EHD brings about large heat transfer coefficients.

Cooper [32] involved in the design of EHD enhanced evaporators, in particular the choices of electrodes and heat transfer surface geometries in Figs. 2.2 and 2.3. For maximum enhancement, the high voltage electrode geometry should be designed such that the maximum field strength was obtained at the heat transfer surface and not in other parts of the system. In addition, heat transfer surface geometry should be such that electric field in homogeneity was maximized in the immediate vicinity of the surface. The presence of intense electric field within the dielectric fluid raised the issue of possible fluid breakdown or chemical charges over prolonged periods of operation.

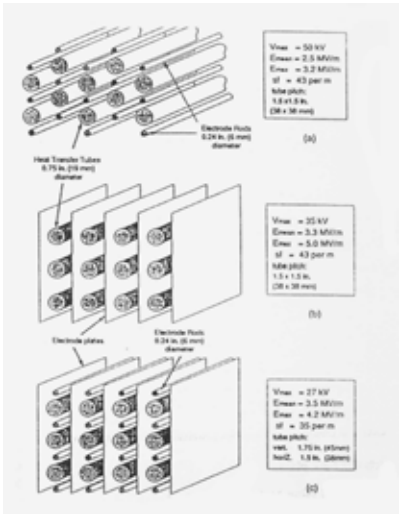

Fig. 2.2 Electrode configurations applicable to EHD shell-and-tube heat exchangers [32].

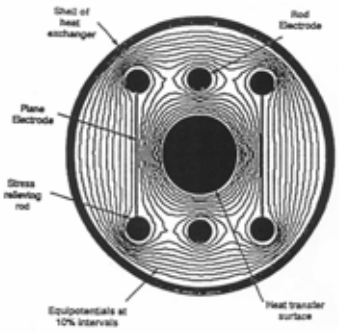

Fig. 2.3 Electric field distributions on a single-tube shell-and-tube heat exchanger [32].

Ogata et al. [33] studied the utilization of EHD boiling augmentation in a tube bundle as shown in Fig. 2.4. R-11 and HCFC-123 were used in this research work. In this test, the boiling heat transfer at a supplied voltage of 18 kV was found to be more than seven times higher than that without an electric field. Moreover, it was found that EHD augmentation of boiling heat transfer in a tube bundle has as effective as in a single tube. The cost calculations suggested that the cost of EHD evaporators is 20-30 % lower than the course of conventional evaporators using low finned or porous tube.

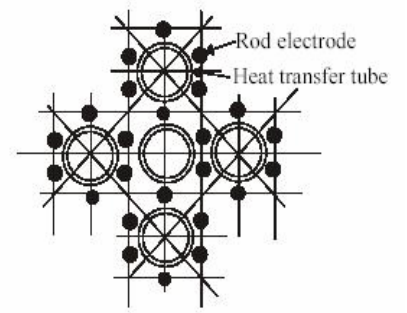

Fig. 2.4 Electrode arrangement around the tube bank [33].

Yeh and Lin [34] investigated the theoretical and experimental work of an effect of collector aspect ratio to the collector efficiency of fiat-plate solar air heater. It was found that with constant collector area, the collector efficiency increases when the collector aspect ratio increases. The theoretical predictions agree reasonably well with experimental results

Allen and Karayiannis [35] reviewed the past work of EHD enhancement heat transfer in single and two-phase heat transfer. Governing equations of electric field, flow field, and temperature field were also included. The three major ways in which EHD can enhance single phase convective heat transfer were corona wind, electrophoresis, and dielectric phoretic forces. It was found that corona wind and electrophoresis gave the highest enhancement ratio, although consideration must be given in the former case to the power consumption and in the latter to the purity and polarity of the medium. A description of the possible practical EHD electrode systems for applications was also presented.

Singh [36] experimentally investigated the EHD technique for in-tube condensation heat transfer enhancement of R-134a. The test section consisted of a horizontally mounted tube-in-tube heat exchanger with refrigerant flowing in the inner tube and water flowing in the outer tube, smooth and microfin copper tubes were tested. Six different electrodes representing various electrode diameters and electrode spacing were used in the apparatus. Up to 640 % improvement in condensation heat transfer coefficient was obtained with the optimum electrode at a maximum EHD power consumption of only 0.08 % of the condenser capacity. The optimum tubes for internal condensation were found to be smooth tubes.

Hachemi [37] introduced the interaction of radiation combined to convection heat transfer. In this effect a flat-plate and two fanned system collectors were selected. The channel back of these collectors was coated in turn by three coverings. In the first a wooden plate only which was the channel back of the collector, in the second and third time a reflecting and a black-painted covering were used, respectively. These were put down on the channel back of collector. The black-painted coating when it was used in the three collectors gives the better improvement followed by the reflecting covering in relation to their respective collectors having uncoated channel back. The greater relative increase of thermal performance was obtained when the flat-plate collector was used and where its channel back was recovered by a black-painted coating.

Karayiannis [38] experimentally studied the heat transfer enhancement of R-132 and R-11 in a shell and tube heat exchanger by using electric field. The test apparatus consisted of five copper tubes as the heat source and four wire electrodes placed around each tube. The range of supplied voltage was 0-25 kV and the heat flux was 5-20 kW/m^2. It was found that the heat transfer enhancement was 930 % at 16 kV supplied voltage and the heat flux was 5 kW/m^2. In the range of 0-15 kV supplied voltage, heat transfer enhancement was linearly proportional to the supplied voltage and lowly off when it higher than 15 kV. It was also found that there was insignificant increase of heat transfer coefficient when the heat flux and the supplied voltage were greater than 10 kW/m^2 and 20 kV, respectively.

Yeh et al. [39] compared the performance of double-flow type solar air heaters, in which air was flowing simultaneously over and under the absorbing plate, which more effective than that of the devices with only one flow channel over or under the absorbing plate because the heat-transfer area in double-flow systems was double. The effect of the fraction of mass flow rate in the upper or lower flow channel of a double-flow device on collector efficiencies had also been investigated theoretically and experimentally. Considerable improvement in collector performance was obtained by employing a double-flow type solar air heater, instead of using a single-flow device, if the mass flow rates in both flow channels were kept the same.

Pottler et al. [40] derived the optimized geometries of solar air heater which shown in Fig. 2.5. As heat transfer augmentation usually increased friction losses, optimum fin

geometry had to be found. For a specific air mass flow rate of 70 kg/(m·h), the air gap for smooth absorbers without fins should be about 7 to 8 mm to get a maximized yearly net energy output of about 2680 MJ/m during the heating season from October through April. Finned absorbers performed much better. Continuous aluminum-fins, 0.1 mm thick and spaced about 6 mm apart in a 30-mm-wide air gap yielded about 900 MJ/m yearly net output. Offset strip fins did not showed an improved performance compared to optimally space continuous fins, due to the larger electrical power for this geometry. However, offset strip fins yielded high net energy gains for large fin spacing.

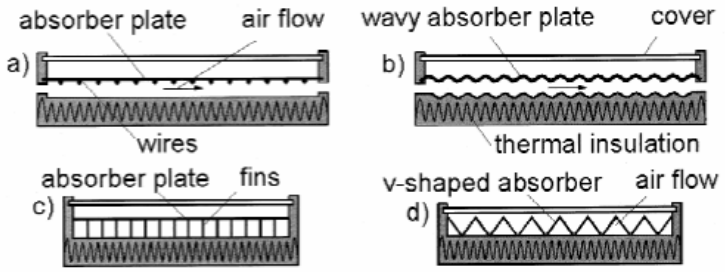

Fig. 2.5 Solar air heaters with heat transfer augmentation [40].

Jiracheewanun et al. [41] studied the heat transfer enhancement and performed flow visualization of air flow through tube bank under electric field. The experimental apparatus consisted of the grounded tube bank of 3x3, 3x6, and 3x9 rows and wire electrodes placed around each tube. The range of supplied voltage was 0-16 kV. It was found that the heat transfer enhancement was 54 % at 16 kV supplied voltage and the Reynolds number was 213. It was also found that electric field showed effective the heat transfer within 12-16 kV supplied voltage.

Verma and Prasad [42] investigated the artificially roughness in the solar air heaters, which perform better than the plane ones under the same operating conditions. Fig. 2.6 shows the results of various parametric ratios of roughness pitch that effected to the flow patterns. Artificial roughness leaded to even more fluid pressure thereby increasing the pumping power. Roughness and flow parameters composed with relative roughness pitch, relative roughness height, and flow Reynolds number have a combined effect on the heat transfer as well as fluid pressure (friction factor). Investigation for the optimal thermohydraulic performance (i.e. maximum heat transfer for minimum friction loss) of

artificially roughness solar air heaters had been carried out. An optimization parameter known as roughness Reynolds number which combines the roughness and flow effect had been considered.

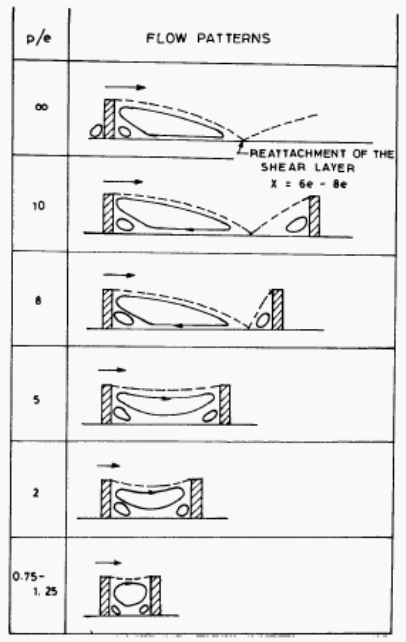

Fig. 2.6 Flow pattern downstream the roughness as a function of pitch [42].

Wangnipparnto et al. [43] studied the airside performance of a thermosyphon heat exchanger with and without the presence of EHD in low Reynolds number region. For the test results without EHD, the predictive ability of the previous correlation significantly under-estimates the present results. With the introduction of EHD, there was significantly increased of heat transfer coefficient when the supplied voltage was higher than 15.5 kV. In the mean time, for a supplied voltage of 17.5 kV, the heat transfer coefficient could be improved by 15% at a Reynolds number of 58. The power consumption relative to the heat transfer rate improvement was within 0.5-20 %.

Yeh et al. [44] Investigated the experimental and analytical works of a design for inserting an absorbing plate to divided the air duct into two channels (the upper and the lower), for double-flow operation in solar air heaters with fins attached over and under the absorbing plate which can illustrated in Figs. 2.7 and 2.8. The present work was restricted to the case where the outside air was being heated directly, and the configuration investigated here will have lower collector efficiency if the inlet-air temperature was

substantially higher than the ambient temperature because of the far greater potential for heat loss from the top. However, the double-flow device introduced here was designed for creating a solar collector with heat-transfer area double between the absorbing plate and heated air. This advantage may compensate for the heat loss from the top when the inlet-air temperature is higher than the ambient temperature. The agreement of the theoretical predictions with those measured values from the experimental results was fairly good. Considerable improvement in collector efficiency of solar air heaters with fins attached was obtained by employing such a double-flow device, instead of using a single-flow example and operating at the same total flow rate. Both the theoretical predictions and experimental results showed that the optimal fraction of airflow rate in upper and lower subchannels was around the value of 0.5. The effect of the flow-rate ratio of the two air streams of flowing over and under the absorbing plate on the enhancement of collector efficiency was also investigated.

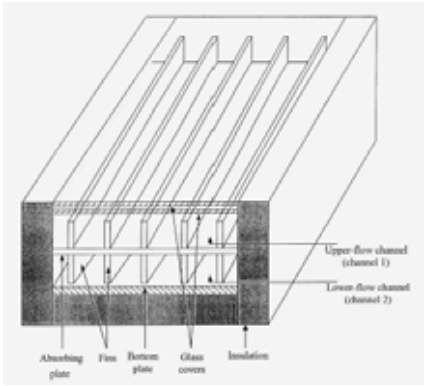

Fig. 2.7 Double-flow solar air heater with fins attached [44].

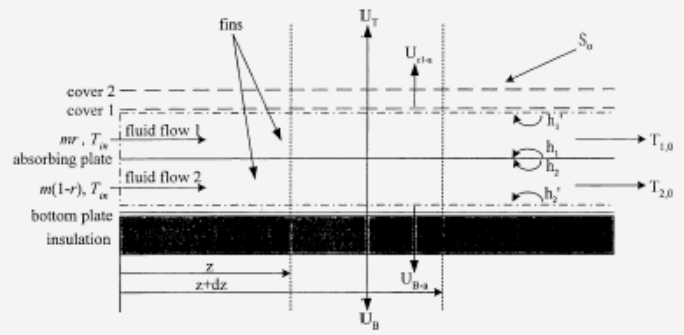

Fig. 2.8 Energy-flow diagram of double-flow solar air heater with fins attached [44].

Momin et al. [45] investigated an experimental work of the effect of geometrical parameters of V-shaped ribs on heat transfer and fluid flow characteristics of rectangular duct of solar air heater with absorbing plate having V-shaped ribs on its underside which represented as Fig. 2.9. The range of parameters for this study had been decided on the basis of practical considerations of the system and operating conditions. The investigation had covered a Reynolds number range of 2500–18000, relative roughness height of 0.02–0.034 and angle of attack of flow of 30–90° for a fixed relative pitch of 10. Results had also been compared with those of smooth duct under similar flow conditions to determine the enhancement in heat transfer coefficient and friction factor. The correlations had been developed for heat transfer coefficient and friction factor for the roughness duct.

Bhagoria et al. [46] performed the experimental study to collect heat transfer and friction data for forced convection flow of air in solar air heater rectangular duct with one broad wall roughness by wedge shaped transverse integral ribs (Fig. 2.10). The experiment encompassed the Reynolds number range from 3000 to 18000, relative roughness height 0.015 to 0.033, and rib wedge angle of 8, 10, 12, and 15°. The effect of parameters on the heat transfer coefficient and friction factor were compared with the result of smooth duct under similar flow conditions. Statistical correlations for the Nusselt number and friction factor had been developed in terms of geometrical parameters of the roughness elements and the flow Reynolds number.

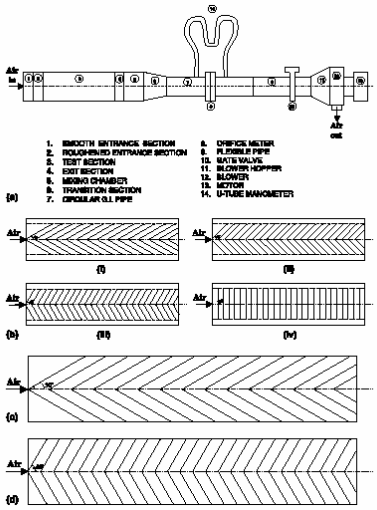

Fig. 2.9 Schematic diagram of experimental setup and roughness elements [45].

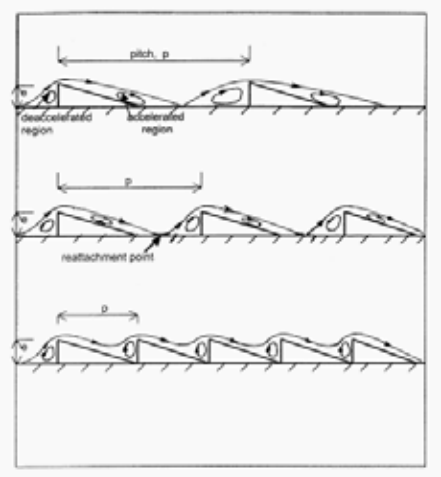

Fig. 2.10 Approximate model of flow patterns for different pitches [46].

2.2 Mathematical Researches

Mathew and Lai [47] presented the numerical results for laminar forced convection in a horizontal channel with two wire electrodes. Attention was also focused on the effect of added electric field on the flow stability. The electric field was generated by positive corona from wire electrodes charged with a DC high voltage between 10-17.5 kV. The Reynolds number considered was in the range of 75-2400. Depending on the EHD number (the ratio between electrical body force and flow inertia), the flow and temperature fields may became steady, periodic, or non-periodic. When the flow inertia was weakened (i.e., a high EHD number), the flow and temperature fields exhibited on oscillatory nature. The oscillation was mainly due to the generation and destruction of multiple recirculation cells. With an increase in the flow velocity, the secondary flow was suppressed and the flow and temperature fields stabilized. The results are illustrated in Figs. 2.11-2.13. It had been shown that an enhancement in heat transfer was possible due to the oscillation of flow field. The maximum enhancement in heat transfer can be as high as six times of that with out the electric field. In addition, it can be observed that the heat transfer enhancement increased with the supplied voltage but decreased with the Reynolds number.

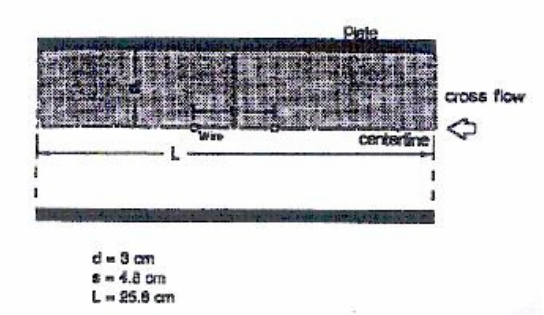

Fig. 2.11 A horizontal channel with two wire electrodes [47].

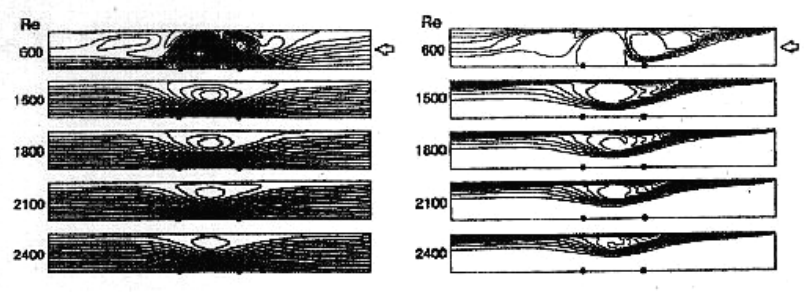

Fig. 2.12 Stable flow and temperature fields for V_0 = 12.5 kV [47].

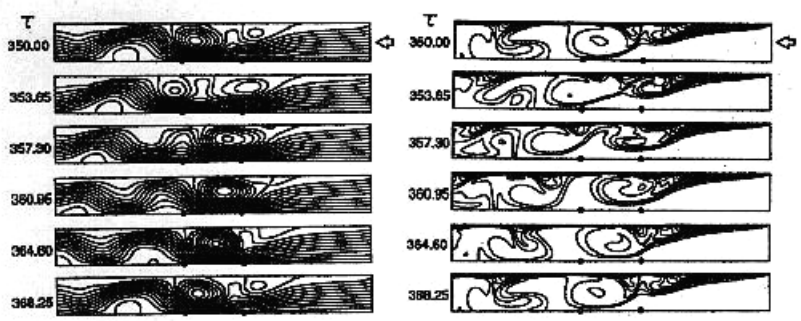

Fig. 2.13 Oscillatory flow and temperature fields for Re = 1200 and V_0 = 12.5 kV [47].

Yadav [48] presented the parametric analysis of a suspended flat plate solar air heater following a transient approach. Fig. 2.14 shows the Schematic diagram of a suspended flat plate solar air heater. An explicit expression for air temperature had been derived as a function of time and the space coordinate. Moreover, explicit expressions were also presented for the glass cover temperature, absorbing plate temperature, useful energy, and efficiency of the proposed system. The effects of several parameters, e.g. space coordinate, mass flow rate, flow velocity, air depth, absorptivity and inlet air temperature on the

performance of the proposed system had also been studied. For appreciation of the analytical results, numerical calculations had been made, and the results were shown graphically.

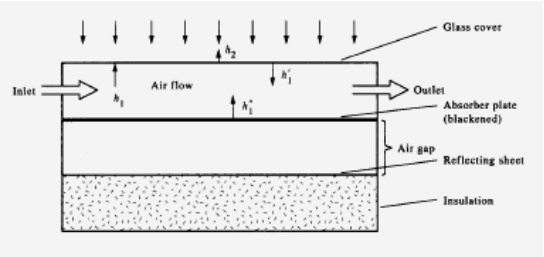

Fig. 2.14 Schematic diagram of a suspended flat plate solar air heater [48].

Goo and Lee [49] developed the numerical scheme to estimate more exactly the collection efficiency of particles in the wire-plate electrostatic precipitator (ESP). The involved physical phenomena such as corona field, turbulent EHD flow field, particle charging, and turbulent motion of particles were treated simultaneously. To overcome the deficiencies of the Eulerian method used up to now, a Lagrangian particle-tracking method coupled with the Monte-Carlo method for simulating the stochastic nature of turbulence was used. With this computational scheme, the characteristics of the ESP were analyzed for a short-length ESP where the effect of developing flow in the entrance region was substantial. The simulation results agreed well with the experimental data, thus it was expected that the characteristics of wire-plate ESP where charging and collection occurs simultaneously can be analyzed using this method without having recourse to a collection efficiency model based on average field characteristics.

Tada et al. [50] studied the theoretical analysis on the enhancement of forced convection heat transfer by applying an electric field. Computational domain was performed in the channel flow where a series of wire electrodes were installed in parallel with the primary flow direction, or installed at right angle to the primary flow direction. It was found that the phenomenon was also performed taking account of momentum transfer between ions and neutral fluid molecules as shown in Figs. 2.15 and 2.16. The enhancement effect of the ionic wind was shown in connection with the operating parameters such as the applied voltage and the primary flow velocity, and the system geometry including the wire electrode arrangement. The application of the ionic wind was

considered to be attractive method of enhancing heat transfer in the low Reynolds number where the application of passive method was not effective.

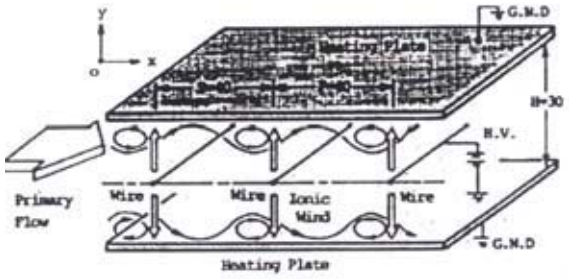

Fig. 2.15 Physical system (cross wire arrangement) [50].

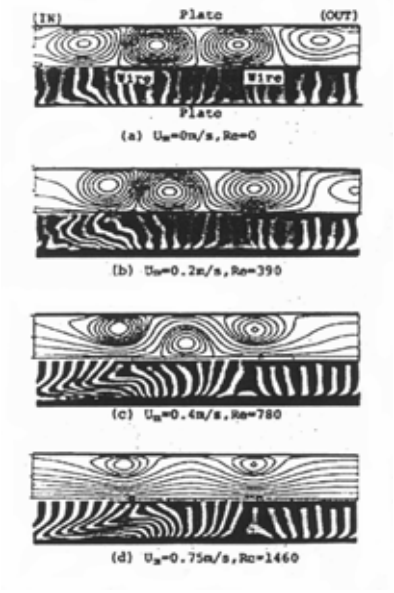

Fig. 2.16 Flow patterns in EHD field (V_0 = 12 kV) [50].

Yang and Lai [51] performed the numerical examination of the heat transfer enhancement using electric field for natural convection in an enclosure. This work was particularly interested on the effects of Joule heating. Attention had also been focused on the stability of the flow and temperature fields under the influence of electric field. Calculations had covered a wide range of parameters 10-17.5 kV supplied voltage and Rayleigh number was in the range of 10^3-10^6, the illustrations are shown in Figs. 2.17-2.19. It was found that Joule heating, although had an additional contribution to heat transfer enhancement at a low Rayleigh number, could result in heat rejection to the hot

wall. The effect of Joule heating diminished as the Rayleigh number increases, but the heat transfer enhancement using electric field also loses its attraction. Therefore, one can concluded that EHD enhanced natural convection was most effective to Rayleigh number in the intermediate range.

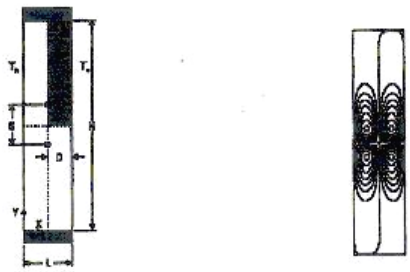

Fig. 2.17 A rectangular enclosure with differentially heated vertical walls and two wire electrodes and the steady flow induced by electric field alone at 15 kV [51].

Fig. 2.18 Flow and temperature fields for natural convection with heat generation at the wires, (a) Ra = 10^4, (b) Ra = 10^5, (c) Ra = 10^6 [51].

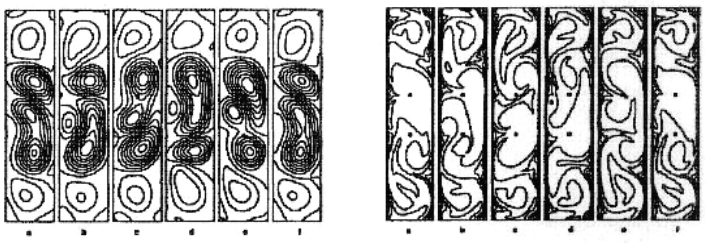

Fig. 2.19 Oscillatory flow and temperature fields at V_0 = 10 kV and Ra = 10 [51].

Badr and Kocabiyik [52] studied the problem of two-dimensional oscillating viscous flow over an elliptic cylinder. The flow was considered incompressible and the free stream oscillations were harmonic. Attention was focused upon only two symmetric flow cases. In the first, flow was symmetric about the major axis whereas in the second, flow was symmetric about the minor axis. The parameters involved were the cylinder axis ratio, Reynolds number, and the oscillation frequency. The major-minor axis ratio of the elliptic cylinder ranges between 1.25 and 2 and the Reynolds number in the range of 500-1000. The methods of solution and numerical scheme were verified by applying them to the special case of an elliptic cylinder starting its constant velocity motion impulsively from rest. The results were compared with the documented translating case, and a good agreement was found. The flow field development was first presented for the two cases of Reynolds number 500 and 1000 in the form of stream line patterns. Comparison between viscous and invicid flow results showed a better agreement for higher values of Reynolds number. Although numerical results were only obtained for harmonic oscillations, the method of solution presented can be applied to free-stream oscillations of any prescribed form.

Lami et al. [53] developed a mathematical model of electric field strength and space charge density in an ESP as

$$q = -\varepsilon\nabla^2 V - q^n - \varepsilon\nabla^2 V^n, \tag{2.1}$$

$$\frac{\partial q}{\partial t} = b\left(\nabla V^n \cdot \nabla q + \nabla q^n \cdot \nabla V\right) + 2\frac{b}{\varepsilon}q^n q = -\frac{b}{\varepsilon}\left(q^n\right)^2 + b\nabla V^n \cdot \nabla q^n. \tag{2.2}$$

The model was based upon the time-dependent, governing equations derived from the classical electrostatic equations on two-dimensional domain. A finite difference method was used to solve numerically the constitute equations. The transient, linear system of equations was discrete on a body-fitted coordinate by mean of analytical development. The body-fitted in orthogonal coordinate system provided accurate solution near the wire with a relatively low number of nodes. The reason for such a behavior was due to the nearly natural alignment of electric field to coordinate lines originating from the wire. The grid selected had the advantage to adjust the nodal spacing over the domain to obtain both good accuracy and economic computer CPU time. Extension of the model to more complicated wire system was also outlined.

Choi and Fletcher [54] studied the behavior of charged particles in turbulent gas flow in ESP as shown in Fig. 2.20 which was crucial information to optimize precipitator efficiency. This work described a strongly coupled calculation procedure for the rigorous computation of particle dynamics during ESP taking into account the statistical particle size distribution which given by

$$\frac{\partial}{\partial x_k}\left(\rho \boldsymbol{v}_i \boldsymbol{v}_k - \left(\mu + \mu_t\right)\frac{\partial \boldsymbol{v}_i}{\partial x_k}\right) = -\frac{\partial P}{\partial x_i} + \boldsymbol{f}_{D_i} + q\boldsymbol{E}_i, \tag{2.3}$$

Ion charge density at the wire was adjusted by the iterative process until the calculated electric field agrees with the value calculated from Peek's formula [55]

$$q^* = q^*\left(\frac{\boldsymbol{E}^n}{\boldsymbol{E}_{Peek}}\right)^{\gamma}, \tag{2.4}$$

$$q^{n+1} = \left(1-\omega\right)q^n + \omega q^*. \tag{2.5}$$

The gas flow was calculated by using the commercial CFD package FLUENT linked to a finite volume solver for the electric field and ion charge. Particle charge density and the particle velocity were averaged in a control volume to use Lagrangian in calculation.

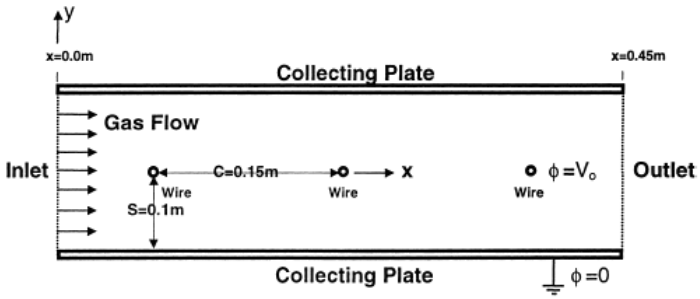

Fig. 2.20 Schematic precipitator geometry [54].

Rafiroiu et al. [56] extended the studied of Peek's formula, which was found to be valid in several simple electrode configuration. The experimental setup specifically modeled the several electrode arrangements. The effect of associating the corona wire to

one or several tubular electrodes of various shapes and sizes was investigated. The experimentally determined corona inception voltage was used as input data of a boundary element method program for the electric field computation. The computed values of the electric field were compared with those given by Peek's formula for wire electrodes of same radius. The derived conclusions can be of help in the custom design of the corona electrode arrangements for various electrostatic applications.

Arulanandam et al. [57] determined the unglazed transpired solar collector effectiveness by computational fluid mechanics (CFD), for conditions of no wind. Because of symmetry, the computational domain needed only to extend over a representative element, which included one hole and the region immediately adjacent to it extending to half the distance between holes. Simulations were carried out over a wide range of conditions, and the results are incorporated into a correlation model. Because of the no-wind assumptions, the model was of limited direct use, but when combined with experimental data, the model could permitted a wider-ranging correlation equation to be obtained.

Hegazy [58] presented a remarkably simple criterion for determining the channel optimum depth-to-length ratio which effectively maximized the useful energy from collectors that were designed to heat a fixed mass rate of air flow. The engineering accuracy of the analytically derived criterion had been corroborated over a wide range of ambient variables, design parameters and operating conditions as shown in Fig. 2.21. The results demonstrated clearly the decisive role of the ratio in enhancing heater performance. A poor choice of this ratio can significantly affect the thermal conversion efficiency, especially for lower specific mass rates. In contrast, decreasing the ratio beyond the optimal value leads to a slight enhancement in heater efficiency. Of significance was the finding that, by choosing optimized value, it also maximized the air temperature rise. For variable flow operation, the ratio of $D/L = 2.5\text{x}10^{-3}$ was recommended as the optimal. Moreover, the reported results and discussions had provided valuable conceptual insights regarding generalization of the performance curves of conventional solar air heaters. It was found that the analytically determined channel depth parameter, in conjunction with the air specific mass rate, were quite successful in correlating the performance in general terms.

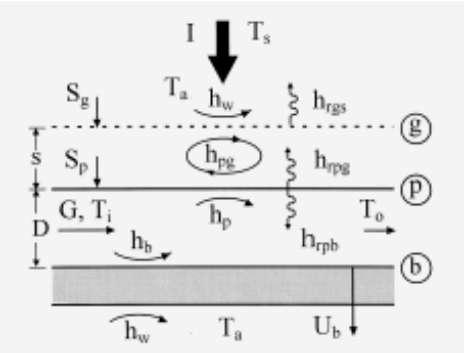

Fig. 2.21 Schematic of conventional solar air heater showing energy balance [58].

Demirel et al [59] studied the characteristics of wall-to-air heat transfer for a fully developed forced convection in a large rectangular packed duct with 160 cm heated length, 40 cm width, and for low bed equivalent diameter to particle diameter ratio. The separation distance between the top and bottom walls was 10 cm. A uniform heat flux was supplied at the top wall, while the bottom wall was insulated. Raschig rings in two and spherical packing in three sizes had been used in the air flow passage to investigate the enhancement of heat transfer due to packing. Temperature profiles for the steady and unsteady states had been measured. In modeling, the Ergun equation and energy equations were solved to calculate the temperature profile for the steady-state only. It was found that the introduction of the packing into the air flow passage increases the wall-to-fluid heat transfer approximately three times compared with that of empty bed. This finding can enhance the rational use of energy from solar air heaters, chemical reactors, electronic cooling and many other engineering applications.

Hilmer et al. [60] developed a method to calculate the short-term dynamic behavior of solar collectors, working with varying fluid-flow rate. It was based on a system of first-order partial differential equations. The method was applied to model a large unglazed collector used for heating a public outdoor swimming-pool in Marburg (Germany). A validation with data measured at this collector showed good short- and long-term accuracy of the model at constant and varying flow rates. Furthermore, the dynamic behavior of the detailed model was compared to that of several model approximations especially at varying flow rate. In the case of unglazed collectors a simple dynamic model, based on an ordinary differential equation, gives accurate results in most practical applications even at varying flow rate. The extension of the method to flat-plate collectors was demonstrated as well.

Gao et al. [61] conducted a numerical study to investigate the natural convection inside the channel between the flat-plate cover and the sine-wave absorber in a cross-corrugated solar air heater (Fig. 2.22). The effects of major system parameters on the natural convection heat transfer were simulated. These parameters including the difference of average temperatures between the cover and the absorber, the characteristic height ratio of the channel which was defined as the ratio of the channel height to the amplitude height of the wavelike absorber, the characteristic geometric ratio which was defined as the ratio of one-fourth of the wavelength to the amplitude height of the absorber, and the angle of inclination of the heater. The numerical results showed that to suppress the natural convection heat loss effectively, the characteristic height ratio should be larger than 2, the characteristic geometric ratio larger than 1, and the angle of inclination less than 40°.

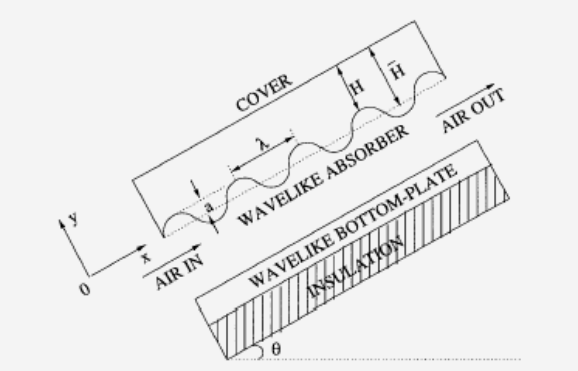

Fig. 2.22 Schematic view of the cross corrugated solar air heater [61].

Talaie et al. [62] presented a new computational scheme that was developed to evaluate current-voltage characteristics of a wire-plate high voltage configuration system applicable for single-stage ESP which was defined such that

$$\frac{\partial\left(qb\boldsymbol{E}_x+\boldsymbol{v}q\right)}{\partial x}+\frac{\partial\left(qb\boldsymbol{E}_y+\boldsymbol{v}q\right)}{\partial y}+\frac{\partial\left(\boldsymbol{v}_p q_p\right)}{\partial x}+\frac{\partial\left(\boldsymbol{v}_p q_p\right)}{\partial y}$$
$$=D_e\left(\frac{\partial^2 q}{\partial x^2}+\frac{\partial^2 q}{\partial y^2}\right)+D_p\left(\frac{\partial^2 q_p}{\partial x^2}+\frac{\partial^2 q_p}{\partial y^2}\right)+S_i \quad . \tag{2.6}$$

This new approach was based on the fact that increasing supplied voltage increases the corona sheath radius. The advantage of this new model compared to previous ones was that the model was capable of computing the rate of corona sheath radius augmentation. Ion charge density at corona edge was calculated by using a new equation, which was developed by dimensional analysis. Also, by using this model, the number of grid points and hence CPU computational time was greatly reduced.

Rafiroiu et al. [63] presented an analysis of the corona field for such electrode arrangements. A corona wind associated with a non-ionizing metallic tube connected to the high voltage and facing a grounded plane was an electrode arrangement frequently encountered in electrostatic processes. The two-loop computational algorithm proposed for the study of this electric field configuration was alternatively solved the Poisson's equation and the equation of charge conservation. Finally, Peek's formula [55] for corona onset was fulfilled.

Ozsunar et al. [64] conducted the numerical analysis of mixed convection heat transfer in rectangular channels under various operating conditions. The lower surface of the channel was subjected to a uniform heat flux, sidewalls were insulated and adiabatic, and the upper surface was exposed to the surrounding fluid. Solutions were obtained for Pr=0.7, inclination angles 0-90°, Reynolds numbers of 50-1000, and modified Grashof numbers of $7x10^5$ to $4x10^6$. The three-dimensional elliptic governing equations were solved using a finite volume based computational fluid dynamics (CFD) code. From a parametric study, local Nusselt number distributions were obtained and effects of channel inclination, surface heat flux and Reynolds number on the onset of instability were investigated. Results obtained from the simulations are compared with the literature and a parallel conducted experimental study, from which a good agreement was observed. The onset of instability was found to move upstream for increasing Grashof number. On the other band, onset of instability was delayed for increasing Reynolds number and increasing inclination angle.

Anagnostopoulos and Bergeles [65] proposed a numerical simulation methodology for calculating the electric field in wire-duct precipitation systems by using finite differencing in orthogonal curvilinear coordinates to solve the potential equation. Charge

density distributions were obtained by the method of characteristics or using a prediction-correction scheme which was given by

$$q_{new}^{n+1} = \left[\frac{1}{q^{(n+1)}} + f_u \left(\frac{1}{q_w^{-(n+1)}} - \frac{1}{q_w^{-(n)}} \right) \right]^{-1} . \tag{2.7}$$

A new mesh generation technique produced body-fitted orthogonal grids, thus the requirements in grid nodes were kept low and the implementation of the method of characteristics became a very easy and fast task. The numerical experiments showed that the commonly used criterion of convergence, which was based on the maximum difference in charge density values between two successive iterations, may not correspond to the remaining error in the field equations. Therefore, its value must be kept properly low in order to avoid erroneous results due to the incomplete convergence.

Gunnewiek et al. [66] extended the earlier study of unglazed transpired-plate solar air heaters (which using a computational fluid dynamics (CFD) model, but that study was limited to the case where there was no wind presented) to the case where there was wind. Large collectors are now routinely built that cover the sides of sizeable buildings (Fig. 2.23), and the problem of designing the system so that the flow of the air through the collector face is reasonably uniform and so that there is no outflow over part of the collector face has been seen as a challenging one. Various building orientations were examined, at a wind speed of 5 m/s. Fig. 2.24 shows the effect of wind direction and it was found to reinforce those factors that tend to produce outflow, and in light of this study, the recommended minimum suction velocity required to avoid outflow has been raised from about 0.0125 m/s to about 0.03 m/s, depending on the building shape. On the other hand, there were possible strategies that could be adopted to reduce the effect of wind, and these were discussed.

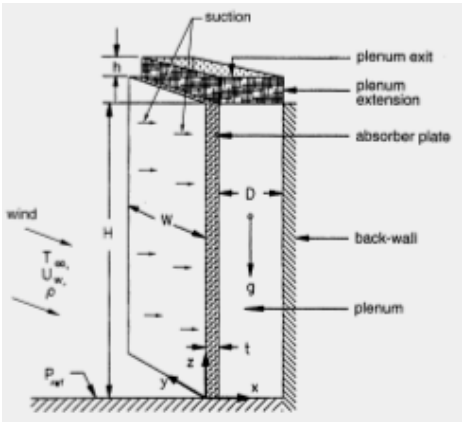

Fig. 2.23 Dimensional sketch of collector's plenum [66].

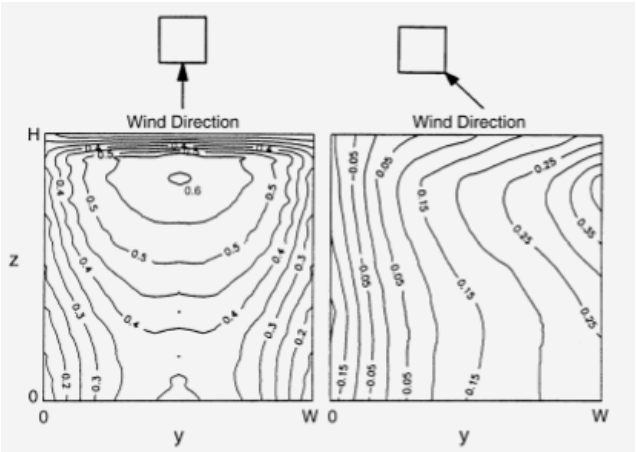

Fig. 2.24 Contour lines of model for the facing directly or quartering wind [66].

Kazeminejad [67] analyzed temperature distribution over the absorbing plate of a parallel flow flat-plate solar collector with one- and two-dimensional steady-state conduction equations with heat generations. The governing differential equations with boundary conditions were solved numerically using a control volume-based finite difference scheme. Comparisons of one- and two-dimensional results showed that the isotherms and performance curve, stated in terms of an effectiveness/number-of-transfer-unit relationship, for one-dimensional analysis slightly deviate from that of two-dimensional analysis, particularly under low mass flow rate conditions. In addition, collector efficiency as a function of operating point was computed and presented graphically for different collector configuration and various operating conditions. For

general engineering purposes, these performance curves may be used for efficient and optimum design of liquid flat-plate solar collectors.

Kasayapanand et al. [68] numerically analyzed the effect of the electrode arrangements in the tube bank on the characteristics of EHD enhanced heat transfer. The numerical modeling of the laminar forced convection includes the interactions among the electric field, flow field, and temperature field. It was found that the heat transfer was significantly enhanced by the EHD at low Reynolds number and the short distance between the wire electrodes and the tube surface from which optimized electrode arrangements were reported for aligned and staggered tube configuration. Moreover, the transformed governing equations could be expressed as;
In the electric field, Poisson equation could be given by

$$\begin{aligned}&\frac{\partial^2 V}{\partial \xi^2}\left[\left(\frac{\partial \xi}{\partial x}\right)^2+\left(\frac{\partial \xi}{\partial y}\right)^2\right]+\frac{\partial^2 V}{\partial \eta^2}\left[\left(\frac{\partial \eta}{\partial x}\right)^2+\left(\frac{\partial \eta}{\partial y}\right)^2\right]+\\&2\frac{\partial^2 V}{\partial \xi \partial \eta}\left[\left(\frac{\partial \xi}{\partial x}\right)\left(\frac{\partial \eta}{\partial x}\right)+\left(\frac{\partial \xi}{\partial y}\right)\left(\frac{\partial \eta}{\partial y}\right)\right]+\\&\frac{\partial V}{\partial \xi}\left[\frac{\partial^2 \xi}{\partial x^2}+\frac{\partial^2 \xi}{\partial y^2}\right]+\frac{\partial V}{\partial \eta}\left[\frac{\partial^2 \eta}{\partial x^2}+\frac{\partial^2 \eta}{\partial y^2}\right]=-\frac{q}{\varepsilon}\end{aligned}\quad , \tag{2.8}$$

and the corona-current continuity equation could be written as

$$q^2=\varepsilon\left[\begin{array}{l}\left[\left[\left(\frac{\partial q}{\partial \xi}\right)\left(\frac{\partial \xi}{\partial x}\right)+\left(\frac{\partial q}{\partial \eta}\right)\left(\frac{\partial \eta}{\partial x}\right)\right]\times\left[\left(\frac{\partial V}{\partial \xi}\right)\left(\frac{\partial \xi}{\partial x}\right)+\left(\frac{\partial V}{\partial \eta}\right)\left(\frac{\partial \eta}{\partial x}\right)\right]\right]+\\\left[\left[\left(\frac{\partial q}{\partial \xi}\right)\left(\frac{\partial \xi}{\partial y}\right)+\left(\frac{\partial q}{\partial \eta}\right)\left(\frac{\partial \eta}{\partial y}\right)\right]\times\left[\left(\frac{\partial V}{\partial \xi}\right)\left(\frac{\partial \xi}{\partial y}\right)+\left(\frac{\partial V}{\partial \eta}\right)\left(\frac{\partial \eta}{\partial y}\right)\right]\right]\end{array}\right]. \tag{2.9}$$

The vorticity transport equation was converted into the form

$$\frac{\partial \boldsymbol{\omega}}{\partial t}=\left[\left[\left(\frac{\partial \psi}{\partial \xi}\right)\left(\frac{\partial \xi}{\partial x}\right)+\left(\frac{\partial \psi}{\partial \eta}\right)\left(\frac{\partial \eta}{\partial x}\right)\right]\times\left[\left(\frac{\partial \boldsymbol{\omega}}{\partial \xi}\right)\left(\frac{\partial \xi}{\partial y}\right)+\left(\frac{\partial \boldsymbol{\omega}}{\partial \eta}\right)\left(\frac{\partial \eta}{\partial y}\right)\right]\right]-$$
$$\left[\left[\left(\frac{\partial \psi}{\partial \xi}\right)\left(\frac{\partial \xi}{\partial y}\right)+\left(\frac{\partial \psi}{\partial \eta}\right)\left(\frac{\partial \eta}{\partial y}\right)\right]\times\left[\left(\frac{\partial \boldsymbol{\omega}}{\partial \xi}\right)\left(\frac{\partial \xi}{\partial x}\right)+\left(\frac{\partial \boldsymbol{\omega}}{\partial \eta}\right)\left(\frac{\partial \eta}{\partial x}\right)\right]\right]+$$
$$\frac{1}{\mathrm{Re}_{EHD}}\left[\begin{array}{l}\dfrac{\partial^2 \psi}{\partial \xi^2}\left[\left(\dfrac{\partial \xi}{\partial x}\right)^2+\left(\dfrac{\partial \xi}{\partial y}\right)^2\right]+\dfrac{\partial^2 \psi}{\partial \eta^2}\left[\left(\dfrac{\partial \eta}{\partial x}\right)^2+\left(\dfrac{\partial \eta}{\partial y}\right)^2\right]+ \\ 2\dfrac{\partial^2 \psi}{\partial \xi \partial \eta}\left[\left(\dfrac{\partial \xi}{\partial x}\right)\left(\dfrac{\partial \eta}{\partial x}\right)+\left(\dfrac{\partial \xi}{\partial y}\right)\left(\dfrac{\partial \eta}{\partial y}\right)\right]+ \\ \dfrac{\partial \psi}{\partial \xi}\left[\dfrac{\partial^2 \xi}{\partial x^2}+\dfrac{\partial^2 \xi}{\partial y^2}\right]+\dfrac{\partial \psi}{\partial \eta}\left[\dfrac{\partial^2 \eta}{\partial x^2}+\dfrac{\partial^2 \eta}{\partial y^2}\right]\end{array}\right]+$$
$$\left[\begin{array}{l}\left[\left[\left(\dfrac{\partial q}{\partial \xi}\right)\left(\dfrac{\partial \xi}{\partial x}\right)+\left(\dfrac{\partial q}{\partial \eta}\right)\left(\dfrac{\partial \eta}{\partial x}\right)\right]\times\left[\left(\dfrac{\partial V}{\partial \xi}\right)\left(\dfrac{\partial \xi}{\partial y}\right)+\left(\dfrac{\partial V}{\partial \eta}\right)\left(\dfrac{\partial \eta}{\partial y}\right)\right]\right]- \\ \left[\left[\left(\dfrac{\partial q}{\partial \xi}\right)\left(\dfrac{\partial \xi}{\partial y}\right)+\left(\dfrac{\partial q}{\partial \eta}\right)\left(\dfrac{\partial \eta}{\partial y}\right)\right]\times\left[\left(\dfrac{\partial V}{\partial \xi}\right)\left(\dfrac{\partial \xi}{\partial x}\right)+\left(\dfrac{\partial V}{\partial \eta}\right)\left(\dfrac{\partial \eta}{\partial x}\right)\right]\right]\end{array}\right] \quad . \quad (2.10)$$

The transformed equation of stream function-vorticity relation could be defined as

$$\begin{array}{l}\dfrac{\partial^2 \psi}{\partial \xi^2}\left[\left(\dfrac{\partial \xi}{\partial x}\right)^2+\left(\dfrac{\partial \xi}{\partial y}\right)^2\right]+\dfrac{\partial^2 \psi}{\partial \eta^2}\left[\left(\dfrac{\partial \eta}{\partial x}\right)^2+\left(\dfrac{\partial \eta}{\partial y}\right)^2\right]+ \\ 2\dfrac{\partial^2 \psi}{\partial \xi \partial \eta}\left[\left(\dfrac{\partial \xi}{\partial x}\right)\left(\dfrac{\partial \eta}{\partial x}\right)+\left(\dfrac{\partial \xi}{\partial y}\right)\left(\dfrac{\partial \eta}{\partial y}\right)\right]+ \\ \dfrac{\partial \psi}{\partial \xi}\left[\dfrac{\partial^2 \xi}{\partial x^2}+\dfrac{\partial^2 \xi}{\partial y^2}\right]+\dfrac{\partial \psi}{\partial \eta}\left[\dfrac{\partial^2 \eta}{\partial x^2}+\dfrac{\partial^2 \eta}{\partial y^2}\right]=-\boldsymbol{\omega}\end{array} \quad , \quad (2.11)$$

and the energy equation was described as

$$\frac{\partial T}{\partial t}=\left[\left[\left(\frac{\partial \boldsymbol{\omega}}{\partial \xi}\right)\left(\frac{\partial \xi}{\partial x}\right)+\left(\frac{\partial \boldsymbol{\omega}}{\partial \eta}\right)\left(\frac{\partial \eta}{\partial x}\right)\right]\times\left[\left(\frac{\partial T}{\partial \xi}\right)\left(\frac{\partial \xi}{\partial y}\right)+\left(\frac{\partial T}{\partial \eta}\right)\left(\frac{\partial \eta}{\partial y}\right)\right]\right]-$$
$$\left[\left[\left(\frac{\partial \boldsymbol{\omega}}{\partial \xi}\right)\left(\frac{\partial \xi}{\partial y}\right)+\left(\frac{\partial \boldsymbol{\omega}}{\partial \eta}\right)\left(\frac{\partial \eta}{\partial y}\right)\right]\times\left[\left(\frac{\partial T}{\partial \xi}\right)\left(\frac{\partial \xi}{\partial x}\right)+\left(\frac{\partial T}{\partial \eta}\right)\left(\frac{\partial \eta}{\partial x}\right)\right]\right]+$$
$$\frac{1}{\mathrm{Re}_{EHD}\times \mathrm{Pr}}\left[\begin{array}{l}\dfrac{\partial^2 T}{\partial \xi^2}\left[\left(\dfrac{\partial \xi}{\partial x}\right)^2+\left(\dfrac{\partial \xi}{\partial y}\right)^2\right]+\dfrac{\partial^2 T}{\partial \eta^2}\left[\left(\dfrac{\partial \eta}{\partial x}\right)^2+\left(\dfrac{\partial \eta}{\partial y}\right)^2\right]+ \\ 2\dfrac{\partial^2 T}{\partial \xi \partial \eta}\left[\left(\dfrac{\partial \xi}{\partial x}\right)\left(\dfrac{\partial \eta}{\partial x}\right)+\left(\dfrac{\partial \xi}{\partial y}\right)\left(\dfrac{\partial \eta}{\partial y}\right)\right]+ \\ \dfrac{\partial T}{\partial \xi}\left[\dfrac{\partial^2 \xi}{\partial x^2}+\dfrac{\partial^2 \xi}{\partial y^2}\right]+\dfrac{\partial T}{\partial \eta}\left[\dfrac{\partial^2 \eta}{\partial x^2}+\dfrac{\partial^2 \eta}{\partial y^2}\right]\end{array}\right] \quad . \quad (2.12)$$

Ammari [69] presented a mathematical model for computing the thermal performance of a single pass flat-plate solar air collector (Figs. 2.25 and 2.26). Air channels were formed by providing metal slats running along the circulated air passage linking the absorbing plate by the bottom one in an endeavor to enhance the thermal efficiency of the solar air collector. A mathematical model, therefore, was developed by which the influence of the addition of the metal slats on the efficiency of the solar collector was studied. A computer code that employed an iterative solution procedure was constructed to solve for the governing energy equations to estimate the mean temperatures of the collector. The effect of volume airflow rate, collector length, and spacing between the absorber and bottom plates on the thermal performance of the present solar air heater was investigated. The results of the comparison had indicated that better thermal performance was obtained by the modified system.

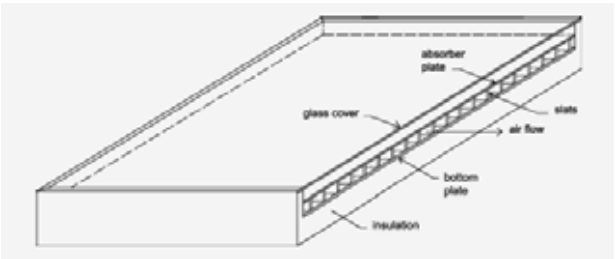

Fig. 2.25 Flat-plate solar air heater with slats [69].

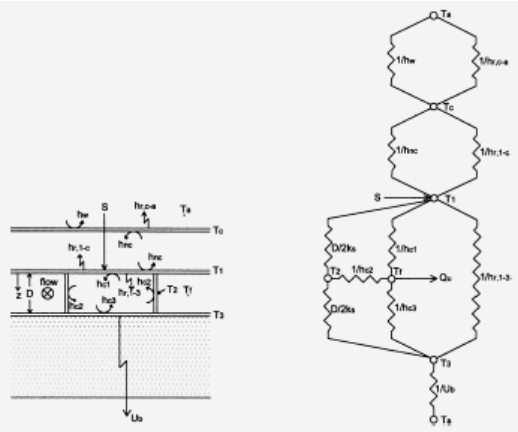

Fig. 2.26 Solar air heater and its thermal network [69].

Abu-Hamdeh [70] developed a mathematical model for predicting thermal efficiency, heat gain, and outlet air temperature of a covered plate attic solar collector under steady conditions. The presented model utilizes the basic principles and relationships of heat transfer was simulated the behavior of the solar air heaters under various conditions. The model was validated by comparing the predicted outlet air temperatures and collector efficiencies to those measured during drying operation of an attic solar collector. The effect of the air speed inside the collector and wind speed above the collector on the collector efficiency were investigated using the mathematical model.

CHAPTER 3 THEORETICAL ANALYSIS

3.1 Fluid Dynamics

The governing equations for the, EHD force $\boldsymbol{F}_E$ per unit volume generated by the electric field with strength $\boldsymbol{E}$ in a fluid of dielectric permittivity ε, density ρ, and uniform temperature T can be expressed as

$$\boldsymbol{F}_E = q\boldsymbol{E} - \frac{1}{2}\boldsymbol{E}^2\nabla\varepsilon + \frac{1}{2}\nabla\left[\boldsymbol{E}^2\left[\frac{\partial\varepsilon}{\partial\rho}\right]_T\rho\right], \tag{3.1}$$

In the symbolic notation, vectors are designated by bold-faced letters, while scalars are denoted by italic letters. Where q is the electric charge density in the fluid. The first term of the right $q\boldsymbol{E}$ is the Coulomb force exerted by electric field upon the free charge or electrophoretic component. While the second and the third term corresponds to the dielectrophoretic and electrostrictive forces on and within the fluid.

By assuming, incompressible flow, incorporating Eq. (3.1) into the conservation of momentum is expressed as

$$\rho\frac{d\boldsymbol{v}}{dt} = \rho\boldsymbol{g} + \boldsymbol{F}_E - \nabla P + \mu\nabla^2 v, \tag{3.2}$$

The vector $\rho\,\boldsymbol{g}$ is the gravitational force per unit volume, P is the local fluid pressure and the last term in the right-hand side of equation represents the viscous terms.
Introducing the vorticity $\boldsymbol{\omega}$ as

$$\boldsymbol{\omega} = \nabla\times\boldsymbol{v}\,, \tag{3.3}$$

the momentum equation can be rewritten in terms of the vorticity defined above as

$$\frac{\partial\boldsymbol{\omega}}{\partial t} + (\boldsymbol{v}\cdot\nabla)\boldsymbol{\omega} = \nu\nabla^2\boldsymbol{\omega} - (\boldsymbol{E}\times\nabla)q\,. \tag{3.4}$$

The stream function (ψ) is defined such that

$$\boldsymbol{v}_x = \frac{\partial \psi}{\partial y},\ \boldsymbol{v}_y = -\frac{\partial \psi}{\partial x}, \tag{3.5}$$

The vorticity transport equation can be obtained from Eqs. (3.4) and (3.5) further gives

$$\nabla^2 \psi = -\boldsymbol{\omega}. \tag{3.6}$$

When attention is brought onto the energy equation of this system, without viscous dissipation effect, the energy equation can be written as

$$\frac{dT}{dt} = \alpha \nabla^2 T + \frac{\sigma_e \boldsymbol{E}^2}{\rho c_p}. \tag{3.7}$$

These systems requires appropriate and sufficient boundary conditions for the flow and temperature fields (for example, in a channel) which are given by

$$x = 0;\ \boldsymbol{\omega} = 0,\ \psi = U_i y,\ T = T_i, \tag{3.8(a))}$$

$$x = L;\ \frac{\partial \boldsymbol{\omega}}{\partial x} = 0,\ \frac{\partial \psi}{\partial x} = 0,\ \frac{\partial^2 T}{\partial x^2} = 0, \tag{3.8(b))}$$

$$y = 0;\ \boldsymbol{\omega} = -\frac{\partial^2 \psi}{\partial y^2},\ \psi = 0,\ \frac{\partial T}{\partial y} = 0, \tag{3.8(c))}$$

$$y = H;\ \boldsymbol{\omega} = -\frac{\partial^2 \psi}{\partial y^2},\ \psi = U_i H,\ \frac{\partial T}{\partial y} = q_h, \tag{3.8(d))}$$

at the channel exit, gradients of stream function, vorticity, and heat flux are set to zero. These boundary conditions are less restrictive and are widely accepted.

Where $\bar{\boldsymbol{n}}$ is the outward perpendicular direction from the wall surface. In addition to the conditions above, a uniform flow is specified at the inlet boundary as well as the non-slip is employed along the surfaces.

3.2 Electrostatic

Maxwell equations for the electric field corresponding to the setup are as the followings

$$\nabla \cdot \varepsilon \boldsymbol{E} = q\,, \tag{3.9}$$

the strength $\boldsymbol{E}$ is given by

$$\boldsymbol{E} = -\nabla V\,. \tag{3.10}$$

As the current is conserved over the domain of calculation, the current continuity equation is given by

$$\nabla \cdot \boldsymbol{J} + \frac{\partial q}{\partial t} = 0\,, \tag{3.11}$$

the current density $\boldsymbol{J}$ is given by

$$\boldsymbol{J} = q\boldsymbol{v} + \sigma_e \boldsymbol{E} + (\boldsymbol{v} \cdot \nabla)(\varepsilon \boldsymbol{E}) - D_e \nabla q\,. \tag{3.12}$$

Combining Eqs. (3.9) with (3.10) and Eqs. (3.11) with (3.12) to eliminate $\boldsymbol{J}$, one can obtain

$$\nabla^2 V = -\frac{q}{\varepsilon}\,, \tag{3.13}$$

$$q^2 = \varepsilon(\boldsymbol{E} \cdot \nabla q)\,. \tag{3.14}$$

The boundary conditions required for solving Eqs. (3.13) and (3.14) are

$V = V_0$, at each wire electrodes, (3.15(a))

$V = 0$, along the surface, (3.15(b))

$\boldsymbol{E}_y = 0$, along the symmetry line. (3.15(c))

Electrical potential and space charge density are determined by iterating Eqs. (3.13) and (3.14) starting with an assumed value of space charge density at the wire electrode (q_0). The validity of the solution is affirmed by comparing the predicted total current to the measured current at the corresponding voltage. If they are different, Eqs. (3.13) and (3.14) will be recalculated by using the new space charge at the wire electrode. The iteration keeps repeating until the convergence is reached.

3.3 Heat Transfer Characteristic

In terms of heat transmission characteristic, the local heat transfer coefficient in term of the local Nusselt number of the laminar sublayer near surface is simply given by

$$\mathrm{Nu}_\theta = \frac{Dh}{k} = \frac{Dq}{k(T_w - T_m)} = \frac{D(\partial T / \partial \overline{\boldsymbol{n}})}{(T_w - T_m)}. \quad (3.16)$$

3.4 Grid Generation

This mathematical model is dealing with the CFD problem of the complex shapes. To solve the problem, the physical shapes of the computational domain are required to arbitrary irregular meshes. One way to bring the boundaries and the finite-difference mesh into alignment is a coordinate transformation. So the non-uniformly spaced grid can be solved on a uniformly spaced grid by using an appropriate transformation. The transformation relations from Cartesian coordinates (x, y) to a general curvilinear system (ξ, η) is calculated by the Poisson's equation.

The transformation of physical plane into computational plane by using grid generation method is shown in Fig. 3.1. In Fig. 3.1(a), the curve meshes are calculated by Poisson's equation including with constrains along the boundary shapes and at the interior of the computational domain. The computed coordinates (x, y) are mapping to evaluated in the orthogonal curvilinear coordinates (ξ, η) by using the transformation relations. Finally,

all governing equations can be solved on a uniformly spaced grid (Fig. 3.1(b)) that is more reliable, efficient, and simpler than that on a non-uniformly spaced grid.

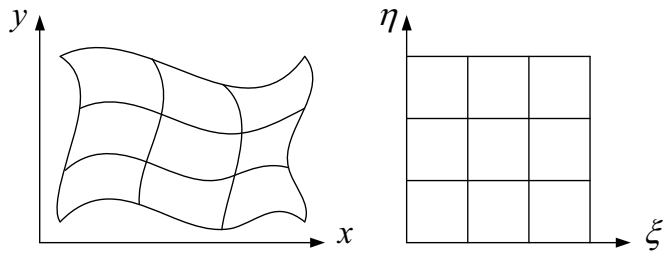

(a) (b)

Fig. 3.1 Physical plane and computational plane.

The relationships among the physical plane and computational plane are

$$\frac{\partial \xi}{\partial x} = J\frac{\partial y}{\partial \eta},\quad \frac{\partial \xi}{\partial y} = -J\frac{\partial x}{\partial \eta},\quad \frac{\partial \eta}{\partial x} = -J\frac{\partial y}{\partial \xi},\quad \frac{\partial \eta}{\partial y} = J\frac{\partial x}{\partial \xi},$$
$$J = \left[\left(\frac{\partial x}{\partial \xi}\right)\left(\frac{\partial y}{\partial \eta}\right) - \left(\frac{\partial x}{\partial \eta}\right)\left(\frac{\partial y}{\partial \xi}\right)\right], \tag{3.17}$$

where curvilinear coordinates (ξ, η) can be solved by Poisson's equations

$$\begin{aligned}
\alpha\frac{\partial^2 x}{\partial \xi^2} - 2\beta\frac{\partial^2 x}{\partial \xi \partial \eta} + \gamma\frac{\partial^2 x}{\partial \eta^2} &= -I^2\left[P\frac{\partial x}{\partial \xi} + Q\frac{\partial x}{\partial \eta}\right] \\
\alpha\frac{\partial^2 y}{\partial \xi^2} - 2\beta\frac{\partial^2 y}{\partial \xi \partial \eta} + \gamma\frac{\partial^2 y}{\partial \eta^2} &= -I^2\left[P\frac{\partial y}{\partial \xi} + Q\frac{\partial y}{\partial \eta}\right]
\end{aligned}. \tag{3.18}$$

The variables used in the previous equations are given by

$$\alpha = \left[\left(\frac{\partial x}{\partial \eta} \right)^2 + \left(\frac{\partial y}{\partial \eta} \right)^2 \right]$$

$$\beta = \left[\left(\frac{\partial x}{\partial \xi} \right)\left(\frac{\partial y}{\partial \eta} \right) + \left(\frac{\partial x}{\partial \eta} \right)\left(\frac{\partial y}{\partial \xi} \right) \right]$$

$$\gamma = \left[\left(\frac{\partial x}{\partial \xi} \right)^2 + \left(\frac{\partial y}{\partial \xi} \right)^2 \right]$$

$$P_{boundary}^{n+1} = P_{boundary}^{n} + \tan^{-1}\left(\frac{\theta^n - \theta^*}{\theta^*} \right)$$

$$Q_{boundary}^{n+1} = Q_{boundary}^{n} + \tan^{-1}\left(\frac{\Delta s^n - \Delta s^*}{\Delta s^*} \right)$$

$$\Delta s = \left(\left(x_{i,j-1} - x_{i,j} \right)^2 + \left(y_{i,j-1} - y_{i,j} \right)^2 \right)^{1/2}$$

$$\Delta t^+ = \left(\left(x_{i+1,j} - x_{i,j} \right)^2 + \left(y_{i+1,j} - y_{i,j} \right)^2 \right)^{1/2}$$

$$\Delta t^- = \left(\left(x_{i,j} - x_{i-1,j} \right)^2 + \left(y_{i,j} - y_{i-1,j} \right)^2 \right)^{1/2}$$

$$\frac{dx}{dt} = \left(\frac{1}{\Delta t^+ + \Delta t^-} \right)\left(\left(\frac{\Delta t^-}{\Delta t^+} \right)\left(x_{i+1,j} - x_{i,j} \right) + \left(\frac{\Delta t^+}{\Delta t^-} \right)\left(x_{i,j} - x_{i-1,j} \right) \right)$$

$$\frac{dy}{dt} = \left(\frac{1}{\Delta t^+ + \Delta t^-} \right)\left(\left(\frac{\Delta t^-}{\Delta t^+} \right)\left(y_{i+1,j} - y_{i,j} \right) + \left(\frac{\Delta t^+}{\Delta t^-} \right)\left(y_{i,j} - y_{i-1,j} \right) \right)$$

$$T_\xi = \left(\frac{x_{i,j-1} - x_{i,j}}{\Delta s} \right) i + \left(\frac{y_{i,j-1} - y_{i,j}}{\Delta s} \right) j \quad . \qquad (3.19)$$

$$T_\eta = \frac{dx}{dt} i + \frac{dy}{dt} j$$

$$\theta = \cos^{-1}\left(\frac{T_\xi \cdot T_\eta}{\left| T_\xi \right| \left| T_\eta \right|} \right)$$

$$P(\xi, \eta) = P(\xi, 1) \cdot e^{-a(\eta-1)/(\eta_{\max}-1)} + P(\xi, \eta_{\max}) \cdot e^{-b(\eta_{\max}-\eta)/(\eta_{\max}-1)}$$

$$Q(\xi, \eta) = Q(\xi, 1) \cdot e^{-c(\eta-1)/(\eta_{\max}-1)} + Q(\xi, \eta_{\max}) \cdot e^{-d(\eta_{\max}-\eta)/(\eta_{\max}-1)}$$

In the electric field, Poisson equation can be given by

$$\begin{aligned}
&\frac{\partial^2 V}{\partial \xi^2}\left[\left(\frac{\partial \xi}{\partial x}\right)^2+\left(\frac{\partial \xi}{\partial y}\right)^2\right]+\frac{\partial^2 V}{\partial \eta^2}\left[\left(\frac{\partial \eta}{\partial x}\right)^2+\left(\frac{\partial \eta}{\partial y}\right)^2\right]+\\
&2\frac{\partial^2 V}{\partial \xi \partial \eta}\left[\left(\frac{\partial \xi}{\partial x}\right)\left(\frac{\partial \eta}{\partial x}\right)+\left(\frac{\partial \xi}{\partial y}\right)\left(\frac{\partial \eta}{\partial y}\right)\right]+ \qquad , \qquad (3.20)\\
&\frac{\partial V}{\partial \xi}\left[\frac{\partial^2 \xi}{\partial x^2}+\frac{\partial^2 \xi}{\partial y^2}\right]+\frac{\partial V}{\partial \eta}\left[\frac{\partial^2 \eta}{\partial x^2}+\frac{\partial^2 \eta}{\partial y^2}\right]=-\frac{q}{\varepsilon}
\end{aligned}$$

and the corona-current continuity equation can be written as

$$q^2=\varepsilon\begin{bmatrix}\left[\left[\left(\frac{\partial q}{\partial \xi}\right)\left(\frac{\partial \xi}{\partial x}\right)+\left(\frac{\partial q}{\partial \eta}\right)\left(\frac{\partial \eta}{\partial x}\right)\right]\times\left[\left(\frac{\partial V}{\partial \xi}\right)\left(\frac{\partial \xi}{\partial x}\right)+\left(\frac{\partial V}{\partial \eta}\right)\left(\frac{\partial \eta}{\partial x}\right)\right]\right]+\\ \left[\left[\left(\frac{\partial q}{\partial \xi}\right)\left(\frac{\partial \xi}{\partial y}\right)+\left(\frac{\partial q}{\partial \eta}\right)\left(\frac{\partial \eta}{\partial y}\right)\right]\times\left[\left(\frac{\partial V}{\partial \xi}\right)\left(\frac{\partial \xi}{\partial y}\right)+\left(\frac{\partial V}{\partial \eta}\right)\left(\frac{\partial \eta}{\partial y}\right)\right]\right]\end{bmatrix}. \quad (3.21)$$

The vorticity transport equation given by

$$\begin{aligned}
&\frac{\partial \boldsymbol{\omega}}{\partial t}=\left[\left[\left(\frac{\partial \psi}{\partial \xi}\right)\left(\frac{\partial \xi}{\partial x}\right)+\left(\frac{\partial \psi}{\partial \eta}\right)\left(\frac{\partial \eta}{\partial x}\right)\right]\times\left[\left(\frac{\partial \boldsymbol{\omega}}{\partial \xi}\right)\left(\frac{\partial \xi}{\partial y}\right)+\left(\frac{\partial \boldsymbol{\omega}}{\partial \eta}\right)\left(\frac{\partial \eta}{\partial y}\right)\right]\right]-\\
&\left[\left[\left(\frac{\partial \psi}{\partial \xi}\right)\left(\frac{\partial \xi}{\partial y}\right)+\left(\frac{\partial \psi}{\partial \eta}\right)\left(\frac{\partial \eta}{\partial y}\right)\right]\times\left[\left(\frac{\partial \boldsymbol{\omega}}{\partial \xi}\right)\left(\frac{\partial \xi}{\partial x}\right)+\left(\frac{\partial \boldsymbol{\omega}}{\partial \eta}\right)\left(\frac{\partial \eta}{\partial x}\right)\right]\right]+\\
&\frac{1}{\mathrm{Re}_{EHD}}\begin{bmatrix}\frac{\partial^2 \psi}{\partial \xi^2}\left[\left(\frac{\partial \xi}{\partial x}\right)^2+\left(\frac{\partial \xi}{\partial y}\right)^2\right]+\frac{\partial^2 \psi}{\partial \eta^2}\left[\left(\frac{\partial \eta}{\partial x}\right)^2+\left(\frac{\partial \eta}{\partial y}\right)^2\right]+\\ 2\frac{\partial^2 \psi}{\partial \xi \partial \eta}\left[\left(\frac{\partial \xi}{\partial x}\right)\left(\frac{\partial \eta}{\partial x}\right)+\left(\frac{\partial \xi}{\partial y}\right)\left(\frac{\partial \eta}{\partial y}\right)\right]+\\ \frac{\partial \psi}{\partial \xi}\left[\frac{\partial^2 \xi}{\partial x^2}+\frac{\partial^2 \xi}{\partial y^2}\right]+\frac{\partial \psi}{\partial \eta}\left[\frac{\partial^2 \eta}{\partial x^2}+\frac{\partial^2 \eta}{\partial y^2}\right]\end{bmatrix}+\\
&\begin{bmatrix}\left[\left[\left(\frac{\partial q}{\partial \xi}\right)\left(\frac{\partial \xi}{\partial x}\right)+\left(\frac{\partial q}{\partial \eta}\right)\left(\frac{\partial \eta}{\partial x}\right)\right]\times\left[\left(\frac{\partial V}{\partial \xi}\right)\left(\frac{\partial \xi}{\partial y}\right)+\left(\frac{\partial V}{\partial \eta}\right)\left(\frac{\partial \eta}{\partial y}\right)\right]\right]-\\ \left[\left[\left(\frac{\partial q}{\partial \xi}\right)\left(\frac{\partial \xi}{\partial y}\right)+\left(\frac{\partial q}{\partial \eta}\right)\left(\frac{\partial \eta}{\partial y}\right)\right]\times\left[\left(\frac{\partial V}{\partial \xi}\right)\left(\frac{\partial \xi}{\partial x}\right)+\left(\frac{\partial V}{\partial \eta}\right)\left(\frac{\partial \eta}{\partial x}\right)\right]\right]\end{bmatrix}, \quad (3.22)
\end{aligned}$$

the transformed equation of stream function-vorticity relation can be written as

$$\frac{\partial^2\psi}{\partial\xi^2}\left[\left(\frac{\partial\xi}{\partial x}\right)^2+\left(\frac{\partial\xi}{\partial y}\right)^2\right]+\frac{\partial^2\psi}{\partial\eta^2}\left[\left(\frac{\partial\eta}{\partial x}\right)^2+\left(\frac{\partial\eta}{\partial y}\right)^2\right]+$$
$$2\frac{\partial^2\psi}{\partial\xi\partial\eta}\left[\left(\frac{\partial\xi}{\partial x}\right)\left(\frac{\partial\eta}{\partial x}\right)+\left(\frac{\partial\xi}{\partial y}\right)\left(\frac{\partial\eta}{\partial y}\right)\right]+ \quad . \qquad (3.23)$$
$$\frac{\partial\psi}{\partial\xi}\left[\frac{\partial^2\xi}{\partial x^2}+\frac{\partial^2\xi}{\partial y^2}\right]+\frac{\partial\psi}{\partial\eta}\left[\frac{\partial^2\eta}{\partial x^2}+\frac{\partial^2\eta}{\partial y^2}\right]=-\boldsymbol{\omega}$$

And the energy equation is expressed as

$$\frac{\partial T}{\partial t}=\left[\left[\left(\frac{\partial\boldsymbol{\omega}}{\partial\xi}\right)\left(\frac{\partial\xi}{\partial x}\right)+\left(\frac{\partial\boldsymbol{\omega}}{\partial\eta}\right)\left(\frac{\partial\eta}{\partial x}\right)\right]\times\left[\left(\frac{\partial T}{\partial\xi}\right)\left(\frac{\partial\xi}{\partial y}\right)+\left(\frac{\partial T}{\partial\eta}\right)\left(\frac{\partial\eta}{\partial y}\right)\right]\right]-$$
$$\left[\left[\left(\frac{\partial\boldsymbol{\omega}}{\partial\xi}\right)\left(\frac{\partial\xi}{\partial y}\right)+\left(\frac{\partial\boldsymbol{\omega}}{\partial\eta}\right)\left(\frac{\partial\eta}{\partial y}\right)\right]\times\left[\left(\frac{\partial T}{\partial\xi}\right)\left(\frac{\partial\xi}{\partial x}\right)+\left(\frac{\partial T}{\partial\eta}\right)\left(\frac{\partial\eta}{\partial x}\right)\right]\right]+$$
$$\frac{1}{\mathrm{Re}_{EHD}\times\mathrm{Pr}}\begin{bmatrix}\frac{\partial^2T}{\partial\xi^2}\left[\left(\frac{\partial\xi}{\partial x}\right)^2+\left(\frac{\partial\xi}{\partial y}\right)^2\right]+\frac{\partial^2T}{\partial\eta^2}\left[\left(\frac{\partial\eta}{\partial x}\right)^2+\left(\frac{\partial\eta}{\partial y}\right)^2\right]+\\ 2\frac{\partial^2T}{\partial\xi\partial\eta}\left[\left(\frac{\partial\xi}{\partial x}\right)\left(\frac{\partial\eta}{\partial x}\right)+\left(\frac{\partial\xi}{\partial y}\right)\left(\frac{\partial\eta}{\partial y}\right)\right]+\\ \frac{\partial T}{\partial\xi}\left[\frac{\partial^2\xi}{\partial x^2}+\frac{\partial^2\xi}{\partial y^2}\right]+\frac{\partial T}{\partial\eta}\left[\frac{\partial^2\eta}{\partial x^2}+\frac{\partial^2\eta}{\partial y^2}\right]\end{bmatrix} \quad . \qquad (3.24)$$

CHAPTER 4 RESEARCH METHODOLOGY

4.1 Calculation Procedure

This research used Mathematica 5.0 program language for calculate electric, flow, and temperature field by finite difference technique. All governing equations can be non-dimensionalized and the numerical calculations have been carried out with the computational grid by using grid generation method to convert the physical plane in Cartesian coordinates (x, y) into the computational plane in curvilinear coordinates (ξ, η) by Poisson's equation. The illustrations of grid generation are shown in Figs. 4.1(a)-(b). In electric field (Fig. 4.1(a)), the first radial discrete value is computed using geometrical progression in such a way to allow high nodal density near the wire and the remaining region being subdivided into equispaced nodes. The starting conic coincides with the wire, for greater distance from the wire, the circular symmetry changes gradually fitting into Cartesian reference at the grounded plates and the symmetrical axes. The obtained charge and potential distributions are converted into polynomial function of quadrilaterals. This function must pass through the values of change and potential distributions at the rectangle nodes and the result can be expressed by interpolation functions. Finally, these values are mapping into computational fluid dynamics grid generation for calculate the velocity and temperature in Fig. 4.1(b). Since the radius of the wire electrode (10^{-4} m) is sufficiently small in the comparison to grid spacing. Therefore, it is allowable to treat the wire electrode as a nodal point. An optimum non-dimensional time step is chosen to ensure numerical stability and accuracy from the grid refinement test.

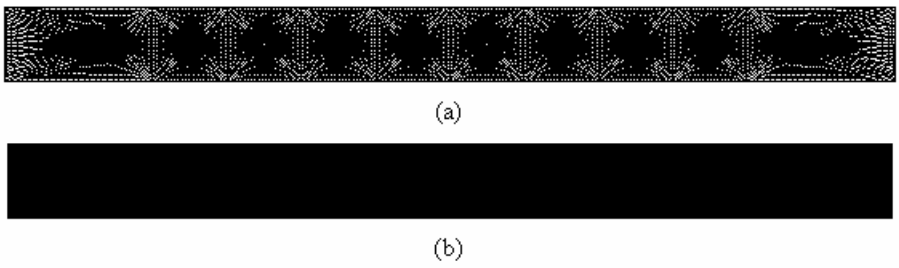

Fig. 4.1 Grid generations.

Several models have been proposed for the calculation of electric field and charge density distribution in a wire-plate electrostatic precipitation system using finite difference method. Firstly, we must assuming q_0 at the wire electrode according to the semi-empirical formula by Peek [55]. The space charged density near the wire can be given by

$$q_0 = \frac{l_w \boldsymbol{J}_P}{\pi brf(30\delta + 0.9(\delta / r)^{1/2})} \times 10^{-5}, \tag{4.1}$$

where δ is T_0P/TP_0, T_0 is 293 K, P_0 is 1.01 × 10^5 N/m^2 , f is 1, T is the operating temperature at 300 K, and P is the operating pressure at 1.01 × 10^5 N/m^2. The $\boldsymbol{J}_P$ is an initial current density at the grounded plate. The detail of calculation procedure is shown in Fig. 4.2 which can be described by

4.1.1 Describe parameters in the program comprising of tube and electrode arrangements, computational dimensions, boundary conditions, initial conditions, and fluid properties.

4.1.2 Convert the physical plane (x, y) in Cartesian coordinates into the computational plane in curvilinear coordinates (ξ, η) by Poisson's equation (Eqs. (3.18) and (3.19)) and set the grid generation.

4.1.3 Assume q_0 at the wire electrode.

4.1.4 The electric field and the charge density distribution are obtained responding to Eqs. (3.20) and (3.21) by successive over relaxation method and finite difference technique, respectively.

4.1.5 Calculate electrical current density around the circumference of tube surface and compared with the experimental results, incorporating with the corona onset by Peek' formula [55] and the theoretical analysis to affirm the accuracy of numerical results.

4.1.6 Embarking an up-wind difference scheme on velocity field at all nodes. The vorticity at each time step is hence obtained from Eq. (3.22), in accordance with the electric field and the stream function obtained from Eq. (3.23).

4.1.7 The temperature field is finally acquired from Eq. (3.24).

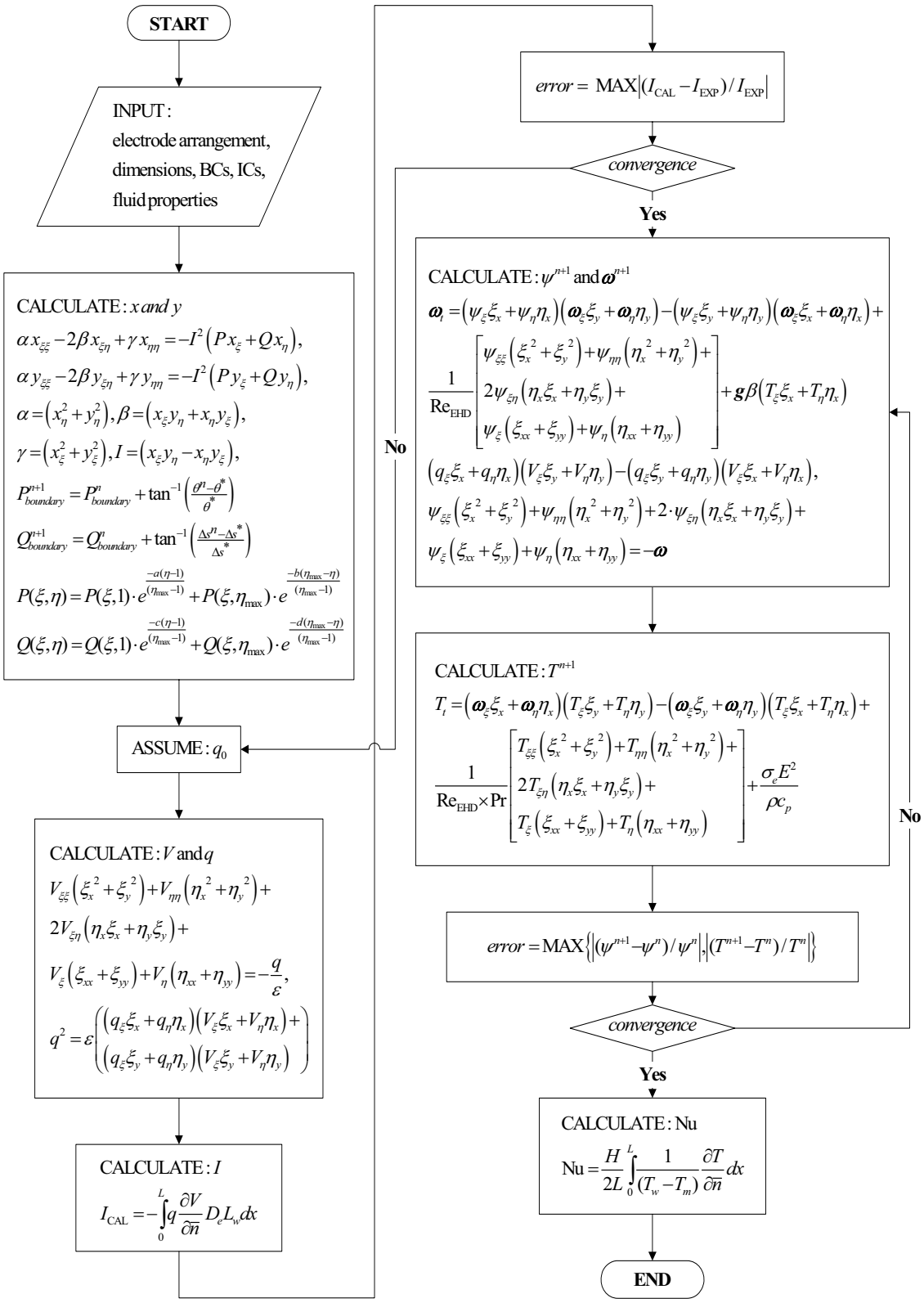

Fig. 4.2 Flow chart for the computational steps.

The above mentioned procedures are repeated until the convergences of stream function and temperature are obtained. The convergence criterion is selected when the deviation of the updated value of each variable calculated from the previous value becomes less than 0.1 percent in case of steady state or the oscillatory occurs in case of periodic state or non-periodic state.

4.2 Range of Parameters

The range of parameters used in the simulation represent in Table 4.1, comprising major parameters, i.e. working fluid, Reynolds number at the inlet, inlet air temperature, supplied voltage at the wire electrode, electrode arrangement, number of electrodes, flow arrangement, polarity of electrode, absorber geometry, boundary condition at an absorbing plate, and channel dimension

Table 4.1 Variables used in the simulation.

Parameter	**Range**
working fluid	air
Reynolds number	100-2000
Rayleigh number	10^4-10^8
inlet air temperature	300-350 K
supplied voltage	0-17.5 kV
electrode arrangement	various categories
number of electrodes	various categories
flow characteristic	natural and forced convections
polarity of electrode	wire is positive and plate is negative
geometry	various categories
BCs at a heated wall	uniform temperature and uniform heat flux
dimensions of domain	various categories

4.3 Experimental Setup

The main equipments are composed with

- High voltage power supply
- Inverter
- Wire electrodes
- Main board controller
- Duct and piping system
- Blower
- Metal plate
- Fin
- Insulator
- Measurement system
- Computer hardware
- Other components

CHAPTER 5 RESULTS AND DISCUSSION

5.1 Channel Configuration

Fig. 5.1 classifies the five categories of electrode arrangement (number of electrodes is fixed at twenty). In case 1, wire electrodes are placed into the upper and lower channels while the number of electrodes remains equally as ten in both channels. Cases 2 and 3 represent the effect of individually installed at upper and lower channel, respectively. Final two categories (cases 4 and 5) investigate the unequal electrodes that separated into fifteen and five electrodes while the distance between electrodes is uniformly distributed along the channel length.

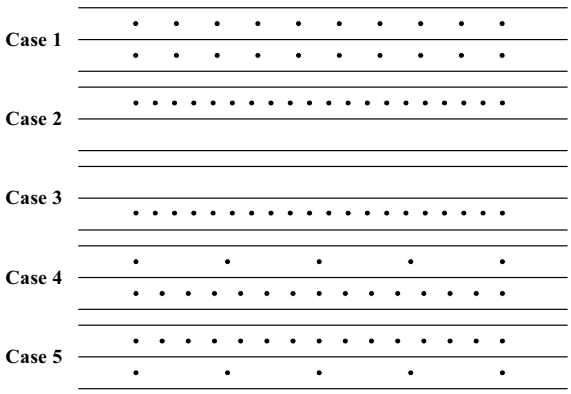

Fig. 5.1 Five categories of the electrode arrangement.

Fig. 5.2 investigates the stream function contours of cases 1-5 of double-flow configuration (this configuration yields the maximum collector efficiency) at $m_U = m_L$ and q = 1000 W/m^2. There is an effect of the secondary flow induced by ionic wind in case 1. Similarly in cases 2 and 3, where the electrodes strip are shifting to the upper and lower, the larger vortices toward the downstream appear closely to the surface especially around the first and last electrodes and its flow patterns are oscillatory in these cases due to the high density of an electric field. In cases 4 and 5, the effect of unequal electrodes density cause the vortices occur along both channels.

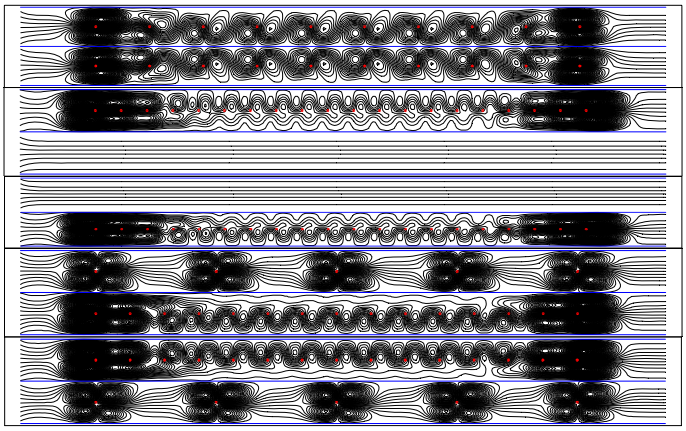

Fig. 5.2 Stream function contours in the double-flow solar air heater (V_0 = 17.5 kV and Re = 100).

Temperature fields (isotherm lines) inside the channels as defined in the previous figure are represented in Fig. 5.3 In case 1, the thermal boundary layer is perturbed by the electric field when it extends over the recirculatory region. High temperature region (or high isotherm lines density) over and under an absorbing plate is smaller compared with the other that cause high heat transfer coefficient. The effect of the electric field plays much important role on the temperature distribution where the number of electrodes is augmented in cases 2 and 3 because of two reasons which are; higher electric field strength due to the many number of electrodes, and many vortices along the channel perform high turbulent mixing which is advantage for convective heat transfer. Nevertheless, high number of electrodes causes the temperature field separated into upper and lower zones with respect to the electrodes strip which conduct the high heat trap along an absorbing plate compared with case 1. For cases 4 and 5, unequal electrodes lead to non-uniform temperature distributions along the channel. Moreover, large vortices from a high number of electrodes at upper channel in case 5 cause the high heat loss on the top as same as in case 2 which affected for augmented collector efficiency of the solar air heater. From these results, the convective heat transfer is consequently depended monotonously with the types of electrode arrangement.

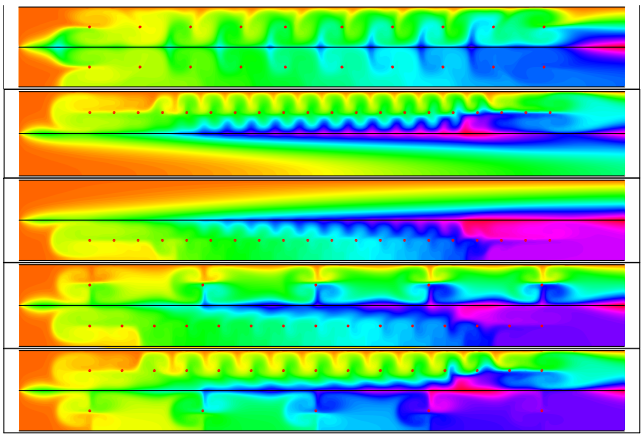

Fig. 5.3 Isotherm lines in the double-flow solar air heater (V_0 = 17.5 kV and Re = 100).

The local heat transfer augmented ratio distributions of five categories of electrode arrangement along the channel which calculated from temperature distributions in Fig. 5.3 have been illustrated in Figs. 5.4 and 5.5. It can be seen that EHD plays much important role on case 1 than other cases. However, the heat transfer received from absorbing plate is not increase in relation with this value due to the large heat loss on the top of collector, while case 3 yields the minimum heat loss because of it does not has electrode at the upper channel.

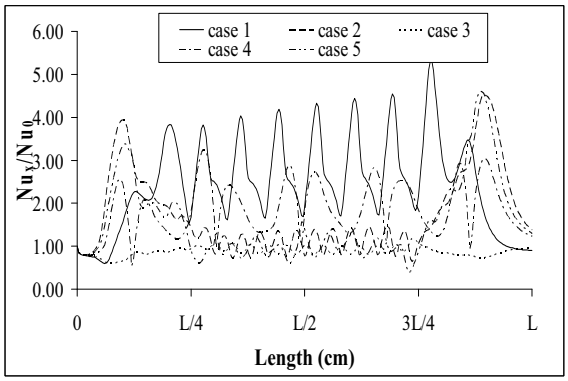

Fig. 5.4 Local heat transfer enhancement along the upper channel (V_0 = 17.5 kV and Re = 100).

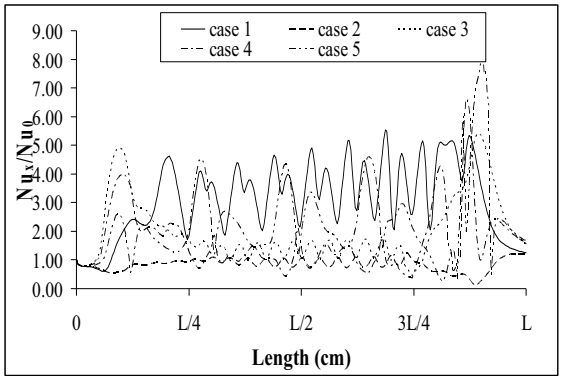

Fig. 5.5 Local heat transfer enhancement along the lower channel (V_0 = 17.5 kV and Re = 100).

Fig. 5.6 conducts the augmented heat transfer distributions of electrode arrangement in case 1 of Fig. 5.1 (simple electrode arrangement) with various Reynolds numbers and supplied voltages. It can be perceived that the ratio of heat transfer enhancement increases in relation with the higher supplied voltage but decreases with the Reynolds number. From above results, that is based on the uniform heat flux condition at an upper plate, which performs enhanced heat transfer coefficient at the same received heat transfer of fluid.

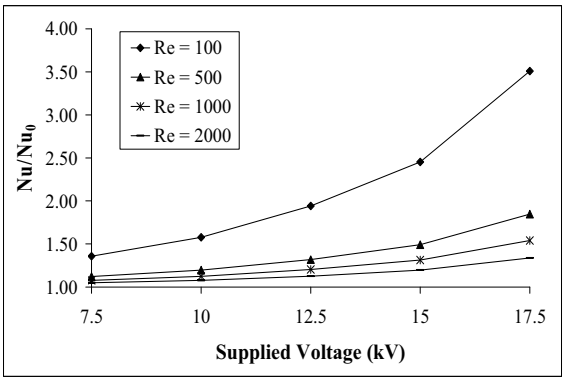

Fig. 5.6 Enhanced ratio at each Reynolds number.

Fig. 5.7 considers an energy profit by assuming uniform temperature of 400 K at an upper plate instead of the previous one. The ratio of the extra received heat transfer of air $\dot{m}c_p\Delta T$ and the electrical power consuming $V_0 I_{CAL}$ is calculated and compared.

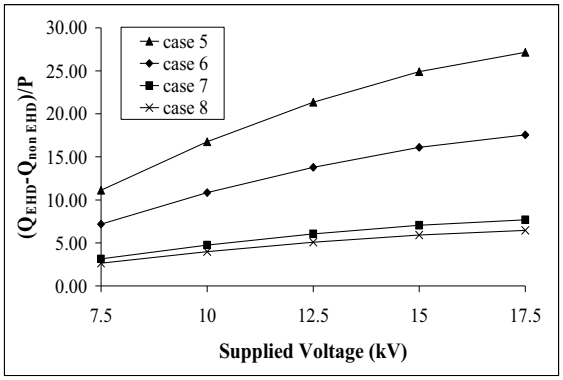

Fig. 5.7 Comparison of heat transfer enhancement per power input (Re = 100).

Fig. 5.8 shows the effect of the channel height on the collector efficiency when the number of electrodes is fixed. As the channel height is less, more electric field strength is given which results in higher heat transfer rate and also the collector efficiency. Nevertheless, the height should not be too small due to the installation problem. Figs. 5.9-5.13 show the effect of a fin array attached in the channels which will be discussed later.

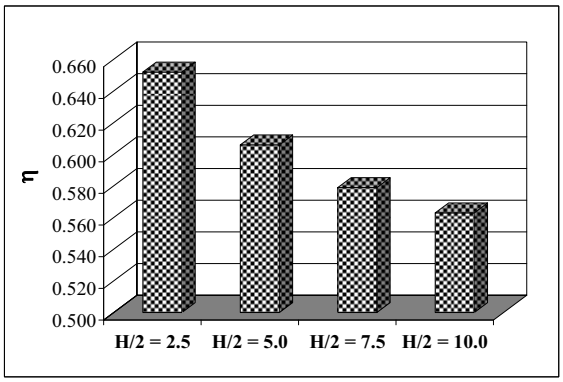

Fig. 5.8 Effect of channel height on the collector efficiency (N = 10 and q = 1000 W/m^2).

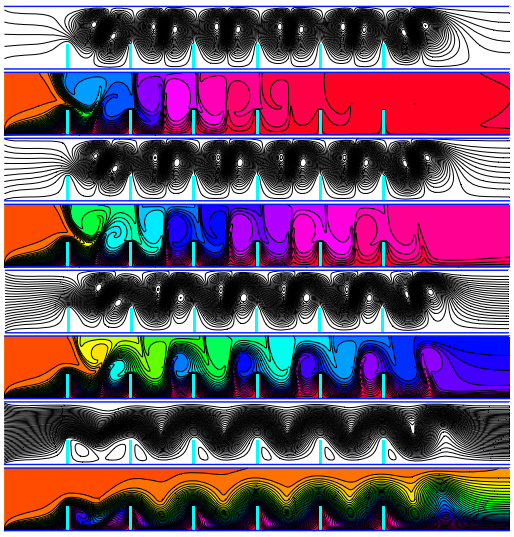

Fig. 5.9 Stream function and isotherm line contours inside the channels for various Reynolds numbers (V_0 = 17.5 kV, N_f = 7, N_e = 7, and L_f = 0.4)

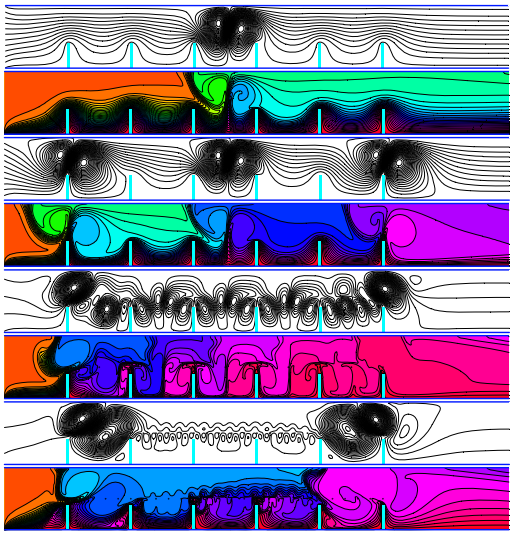

Fig. 5.10 Number of electrodes effect on the flow and temperature fields inside the finned channels (V_0 = 17.5 kV, Re = 100, N_f = 7, and L_f = 0.4)

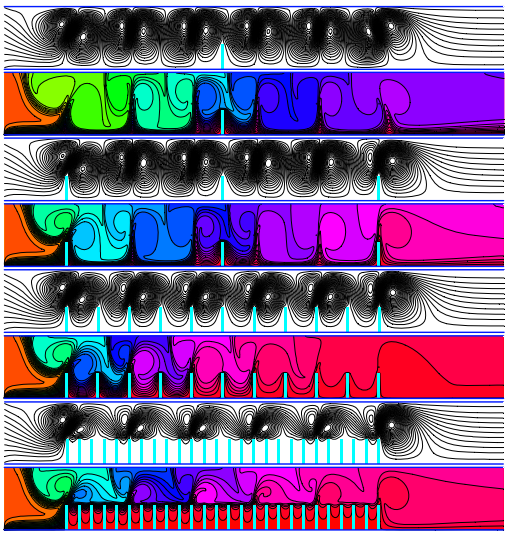

Fig. 5.11 Number of fins effect on the flow and temperature fields inside the finned channels (V_0 = 17.5 kV, Re = 100, N_e = 7, and L_f = 0.4)

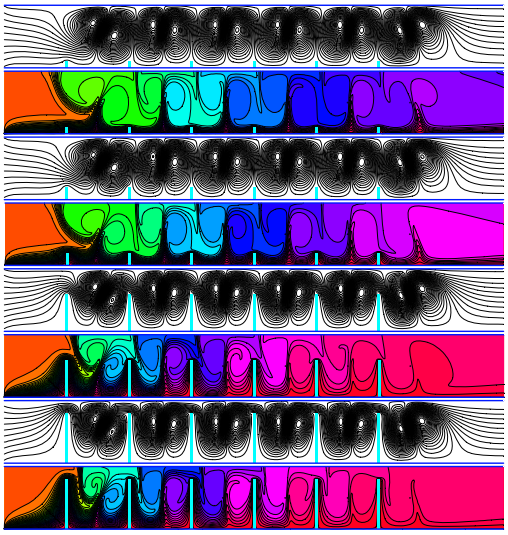

Fig. 5.12 Stream function and isotherm line contours inside the finned channels for various fin lengths (V_0 = 17.5 kV, Re = 100, N_f = 7, and N_e = 7)

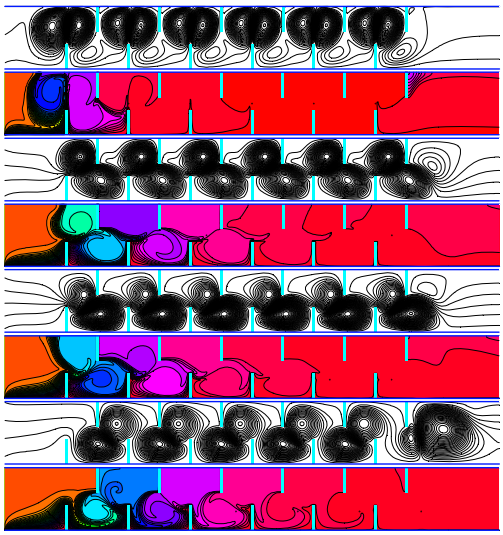

Fig. 5.13 Effect of the electrode arrangement on the flow and temperature fields (V_0 = 17.5 kV, Re = 100, N_f = 14, N_e = 7, and L_f = 0.4)

5.2 Enclosure Configuration

The enclosure domain and boundary conditions are conducted in Fig. 5.14 The right thermally conducting plate is maintained at a uniform heat flux, and the left thermally conducting plate is maintained at a uniform temperature of 300 K. Both upper and lower plates are thermal insulators. All plates are electrically grounded, and the enclosure has a size of 5 × 40 cm^2. Fig. 5.15 shows the stream function contours obtained by applying the EHD effect while the Rayleigh number is varied between 10^4 and 10^8. In the latter cases, the effect of Joule heating at the wire electrode is negligible (V_0 = 17.5 kV, N = 7). There is an effect of the secondary flow induced by the ionic wind at the wire electrode, which causes four rotating cellular motions at each electrode in Fig. 5.15(a). The Rayleigh number is next increased further, until the fluid inside the enclosure is dominated by the effect of Rayleigh number instead of the electric field. The flow patterns are oscillatory due to the interaction between the thermal buoyancy force and electrical body force. Two categories of oscillation -- the periodic state of Figs. 5.15(a) and (b), and the non-periodic state of Figs. 5.15(c)-(e) -- are observed in these figures. Fig. 5.16 presents the temperature fields (isotherm lines) inside the enclosures defined in Fig. 5.15. The thermal boundary layer is perturbed by the electric field when it extends over the recirculation region. It can be seen that the temperature gradient, represented by the line density, at the right plate

becomes larger with an increasing Rayleigh number, resulting in a high heat transfer coefficient. It can be concluded that for low Rayleigh number, the flow and temperature fields have been substantially affected by an electric field. However, the effect of EHD is diminished at high Rayleigh number which is an indication of no significant change in heat transfer enhancement.

The oscillatory stream function and isotherm line contours for 3, 7, 13, 26, and 51 electrodes are shown in Figs. 5.17 and 5.18 (V_0 = 17.5 kV, Ra = 10^6). Altering the number of electrodes causes different flow patterns to occur in the enclosure. The number of vortices is seen to increase when the number of electrodes is augmented from 3 to 13, but remains relatively constant as the number of electrodes increases to 26 and 51. Large vortices appear at the upper and lower zones of the enclosures of Figs. 5.17(d) and (e), especially around the extremes of the electrode strips, due to the low pressure region. The temperature gradient along the right plate of Fig. 5.18(e) is highest in comparison to other configurations that cause the maximum heat transfer coefficient to be a maximum. One can thus conclude that the effect of the number of electrodes is more significant at larger number values. This effect should be considered together with the extra heat transfer per unit input power of electrical energy for optimization.

A comparison of the average heat transfer enhancement over a cycle of the periodic state, or over the entire time span of the non-periodic state, along an enclosure is shown for various Rayleigh numbers in Fig. 5.19 (N = 7). The latter is evaluated using the ratio of the average Nusselt number in the presence of an electric field to that without an electric field. The results show that EHD enhancement of flow and heat transfer plays an important role in regions of low Rayleigh number, while convective heat transfer is consequently dependent on the relation between Rayleigh number and supply voltage. Fig. 5.20 demonstrates the relationship between heat transfer enhancement and number of electrodes for V_0 = 17.5 kV. The enhancement ratio reaches a minimum at an intermediate number of electrodes (the combination between oscillatory cells occurs here) and increases again due to the high intensity of the electric field at higher numbers of electrodes. This phenomenon can be described by considering the isotherm line density at the right plate of Fig. 5.18(a). For the case N = 3, the density is found to be higher than for N = 7 due to the lower number of vortices and also the smaller heat trap that yields a higher heat transfer coefficient. Since the number of electrodes is rather high at N = 13, 26, and 51, many vortices are formulated along the domain of enclosure, and they combine when the number of electrodes is large, even though there is good turbulent mixing. The flow and temperature fields are

recirculating and oscillating, especially around the top and bottom zones of the enclosure. Therefore, the heat transfer coefficient is augmented due to the larger ionic wind effect. Thus, the optimum number of electrodes installed in an enclosure is significantly affected.

The enhanced ratio between average fluid velocity inside the enclosure and various numbers of electrodes, averaged along the computational domain and over a period or an entire time span, is investigated in Fig. 5.21 for V_0 = 17.5 kV. The velocity enhancement increases monotonically with the number of electrodes. A comparison between Figs. 5.20 and 5.21 shows that the velocity enhancement does not display a similar tendency and the heat transfer enhancement, instead increasing further with number of electrodes, while the augmentation to heat transfer shows a minimum value at an intermediate number of electrodes.

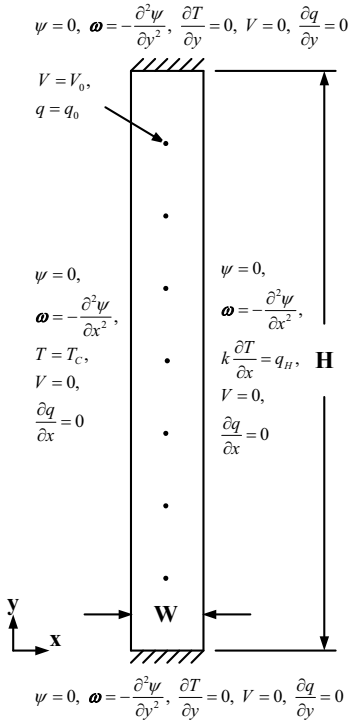

Fig. 5.14 Boundary conditions and generated grid.

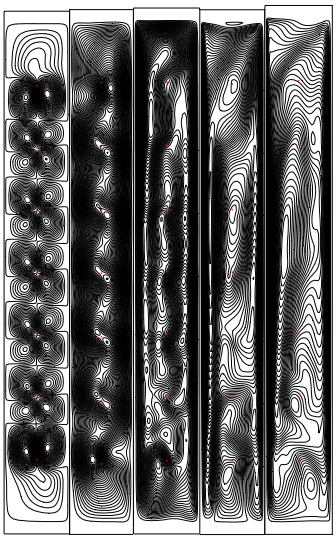

(a) (b) (c) (d) (e)

Fig. 5.15 Stream function contours inside enclosure for various Rayleigh numbers (V_0 = 17.5 kV, N = 7): (a) Ra = 10^4, (b) Ra = 10^5, (c) Ra = 10^6, (d) Ra = 10^7, and (e) Ra = 10^8.

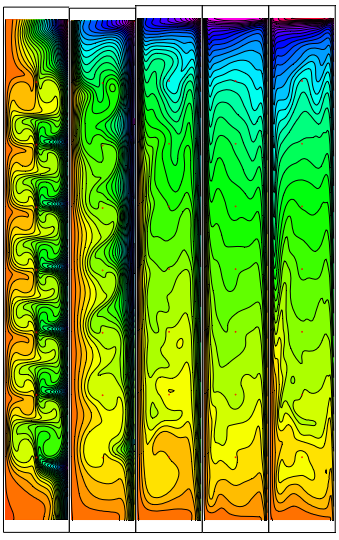

(a) (b) (c) (d) (e)

Fig. 5.16 Temperature distributions inside enclosure for various Rayleigh numbers (V_0 = 17.5 kV, N = 7): (a) Ra = 10^4, (b) Ra = 10^5, (c) Ra = 10^6, (d) Ra = 10^7, and (e) Ra = 10^8.

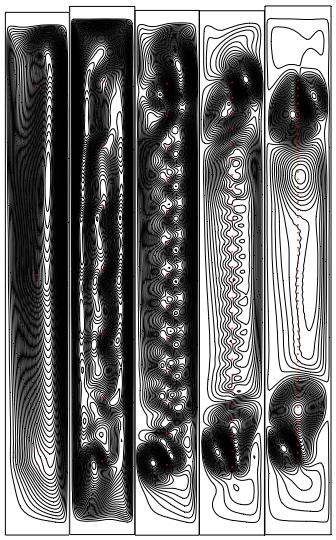

(a) (b) (c) (d) (e)

Fig. 5.17 Stream function contours inside enclosure for various numbers of electrodes (V_0 = 17.5 kV, Ra = 10^6): (a) $N = 37$, (b) $N = 7$, (c) $N = 13$, (d) $N = 26$, and (e) $N = 51$.

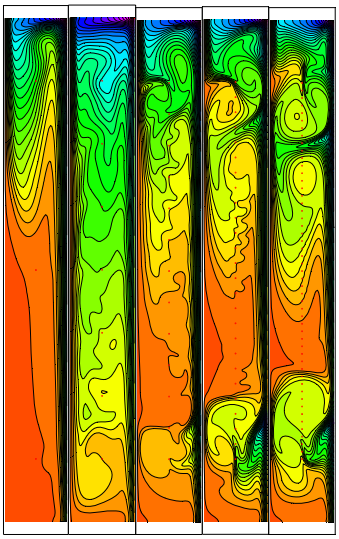

(a) (b) (c) (d) (e)

Fig. 5.18 Temperature distributions inside enclosure for various numbers of electrodes (V_0 = 17.5 kV, Ra = 10^6): (a) $N = 37$, (b) $N = 7$, (c) $N = 13$, (d) $N = 26$, and (e) $N = 51$.

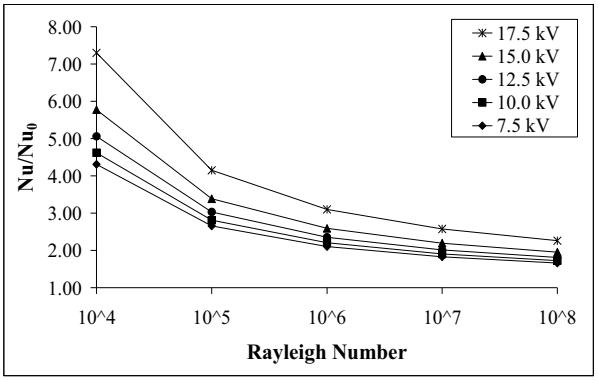

Fig. 5.19 Heat transfer enhancement in relation to supply voltage (N = 7).

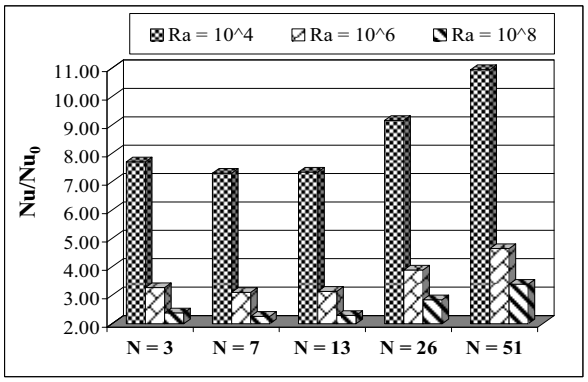

Fig. 5.20 Effect of number of electrodes to the heat transfer augmentation (V_0 = 17.5 kV).

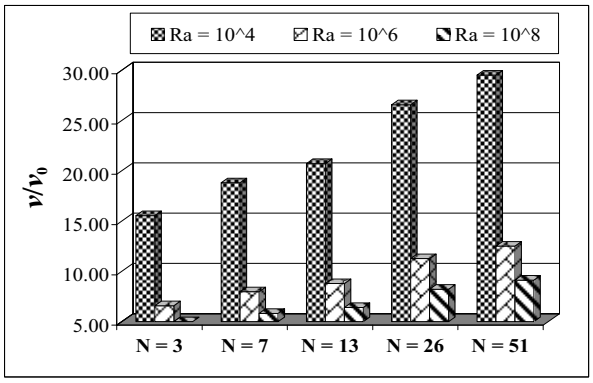

Fig. 5.21 Average velocity enhancement for various numbers of electrodes (V_0 = 17.5 kV).

Fig. 5.22 investigates the stream function and isotherm line contours inside the cavities with multiple fins attached uniformly on the left plate (V_0 = 12.0 kV, N_f = 7, N_e = 1, L_f = 0.25, and $W \times H$ = 15 × 15 cm^2): (a) Ra = 10^4, (b) Ra = 10^5, (c) Ra = 10^7, and (d) Ra = 10^8 while the Rayleigh numbers is varied from 10^4 to 10^7, in which the effect of Joule heating at the wire electrode is neglected. Since the Boussinesq approximation is adopted in this study, the energy equation does affect the momentum equation. For non-EHD, the fluid creates a clockwise rotating cellular motion. At low Rayleigh number, the strength of the primary vortex is weakened due to the fins obstruct movement of the fluid. This is because the convection not being strong compared with conduction and it has the most remarkable effects on the flow field when they are placed at the middle of the left plate. It appears that the stream lines become more packed with the increasing of Rayleigh number, thus, the fluid moves faster as natural convection is intensified. For applying EHD (an electrode is positioned at the center of enclosure), there is an effect of the secondary flow induced by the ionic wind at the wire electrodes, which causes two rotating cellular motions in Fig. 5.22(a). In next cases, where the Rayleigh number is increased further, fluid inside the enclosure is dominated by the effect of Rayleigh number instead of the electric field. The flow patterns are oscillated due to the interaction between the thermal buoyancy force and electrical body force. The thermal boundary layer is perturbed by the electric field when it extends over the recirculation region. It can be concluded that for low Rayleigh number, the flow and temperature fields have been substantially affected by the electric field. However, the effect of EHD is diminished at high Rayleigh number which can be indicated that no significant change in the heat transfer enhancement.

Fig. 5.23 conducts the flow and temperature fields with the multiple fins attached while the electrodes are placed at the middle (electrode strip is installed at the middle of enclosure in x direction and each electrode is positioned on the line of fin length in y direction), extreme (electrode strip is installed near the end of fin in x direction and each electrode is positioned on the line of fin length in y direction), top-extreme (electrode strip is installed near the end of fin in x direction and each electrode is positioned between the line of fin length in y direction), and top (electrode strip is installed at the middle of fin length in x direction and each electrode is positioned between the line of fin length in y direction) arrangements, respectively, in which the numbers of fins and electrodes are kept the same at seven (V_0 = 12.0 kV, Ra = 10^6, N_f = 7, N_e = 7, L_f = 0.25, and $W \times H$ = 15 × 15 cm^2): (a) (x = 7.5 cm, y is on the line of fin length), (b) (x = 4.6875 cm, y is on the line of fin length), (c) (x = 4.6875 cm, y is between the line of fin length), and (d) (x = 1.875 cm, y

is between the line of fin length). It can be observed that the top arrangement positioned yields the multiple vortices which reduce the flow structure, while the extreme arrangement performs a maximum average velocity from the high velocity along the hot plate compared with other arrangements. For temperature field, it can be observed that the extreme arrangement still obtains the highest temperature gradient along the hot wall.

A non-equivalent number of fins causes different flow patterns to occur in the enclosure of Fig. 5.24 (V_0 = 12.0 kV, Ra = 10^6, N_e = 1, L_f = 0.25, and $W \times H$ = 15 × 15 cm^2): (a) N_f = 2, (b) N_f = 4, (c) N_f = 9, and (d) N_f = 15. It can be observed that the separation over the fin appears especially at the top zone of the enclosure. As seen that temperature gradient along the left plate of Fig. 5.24(a) is highest compared with other categories that may results in maximum heat transfer coefficient. In Fig. 5.25 (V_0 = 12.0 kV, Ra = 10^6, N_f = 1, N_e = 2, and $W \times H$ = 15 × 15 cm^2): (a) L_f = 0.0625, (b) L_f = 0.125, (c) L_f = 0.5, and (d) L_f = 0.75, the enclosure is divided in upper and lower zones which each zone has one electrode located at the center. The presence and the character of the primary clockwise rotating vortex is unaltered, with a longer fin bringing about more changes to the flow compared to a shorter fin. It is noticed that for $L_f \geq 0.5$ (Fig. 5.25(b) and (c)), many recirculating vortices are found above the fin and under the top insulated wall. The longer fin has more remarkable effects on the flow fields. Comparing Figs. 5.25(a) and (b) along fin at most positions only changes the temperature distribution locally and the rest of the enclosure remains unaffected. This is because the primary vortex has not altered too much upon introduction of a short fin and the fin only changes the velocity distribution locally.

The average Nusselt number along the enclosures for various Rayleigh numbers is shown in Fig. 5.26 (V_0 = 12.0 kV, N_f = 7, N_e = 1, L_f = 0.25, and $W \times H$ = 15 × 15 cm^2). For non-EHD, placing fins on the left plate always reduces the heat transfer on the left plate. The average Nusselt number of the left plate becomes smaller with an increasing of the fin length due to the fins obstruct flow and also reduce convective strength. However, the effect of fins becomes less remarkable with the rising of the Rayleigh number because the primary flow is enhanced with compensate the effect of blocking by the fins. Thus, for high Rayleigh number, the flow field is augmented regardless of the length and position of fins. Therefore, it is found that EHD augmented flow and heat transfer play much important role at the low Rayleigh number region, and this phenomenon is consequently influenced at the high supplied voltage.

In Fig. 5.27, one can see that the effect of the previous electrode arrangement on the multiple fins becomes more remarkable with the rising of the Nusselt number due to the

fact that it has minimum thermal boundary layer thickness along the fin. Fig. 5.28 demonstrates the relation between heat transfer enhancement and number of fins (V_0 = 12.0 kV, N_e = 1, L_f = 0.25, and $W \times H$ = 15 × 15 cm^2). Thus, augmented Nusselt number increases monotonously with the number of fins due to the low convective heat transfer in non-EHD phenomenon that described in Fig. 5.24. In Fig. 5.29 (V_0 = 12.0 kV, N_f = 1, N_e = 2, and $W \times H$ = 15 × 15 cm^2), it is observed that for a fin placed at a fixed position, the local Nusselt number near the fin decreases with the increase of fin length. For shorter fin, the fin has very little influence on the area that is far from the fin. For example, for a fin at L_f = 0.0625 (Fig. 5.25(a)), the local Nusselt number distribution at the bottom of the left plate is very close to the case without a fin. Even though a long fin attached on the left plate always reduces the heat transfer on the left plate. As expected, one can see that placing a fin on the left plate has most remarkable EHD effects on the augmented Nusselt number on the hot wall with the increase of fin length.

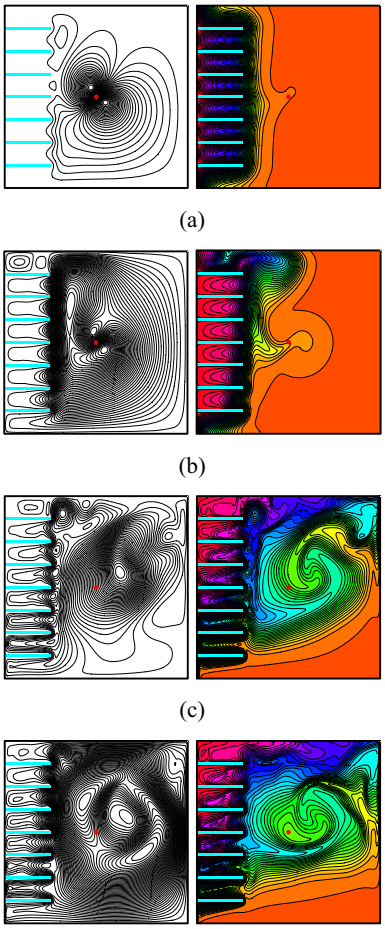

Fig. 5.22 Effect of the Rayleigh number on the flow and temperature fields (V_0 = 12.0 kV, N_f = 7, N_e = 1, L_f = 0.25, and $W \times H$ = 15 × 15 cm^2): (a) Ra = 10^4 ($\Delta\bar{\psi}$ = 5.0 × 10^{-5}, $\Delta\theta$ = 2.5 × 10^{-2}), (b) Ra = 10^5 ($\Delta\bar{\psi}$ = 1.0 × 10^{-4}, $\Delta\theta$ = 2.5 × 10^{-2}), (c) Ra = 10^7 ($\Delta\bar{\psi}$ = 4.0 × 10^{-4}, $\Delta\theta$ = 2.5 × 10^{-2}), and (d) Ra = 10^8 ($\Delta\bar{\psi}$ = 8.0 × 10^{-4}, $\Delta\theta$ = 2.5 × 10^{-2}).

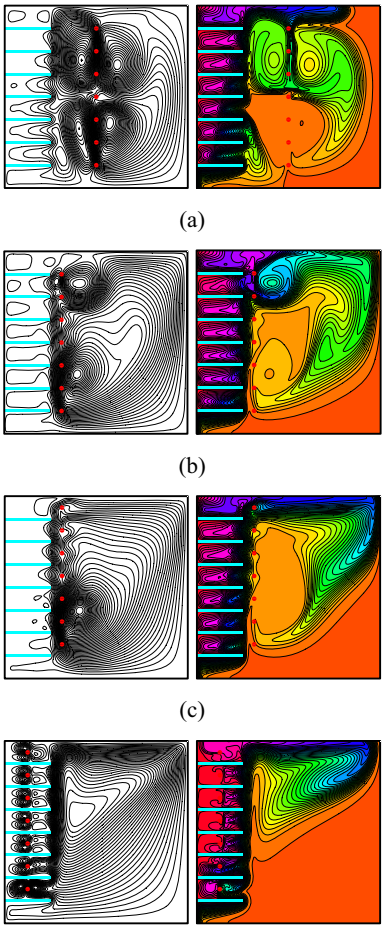

Fig. 5.23 Electrode arrangement effect on the flow and temperature fields of the multiple fins (V_0 = 12.0 kV, Ra = 10^6, N_f = 7, N_e = 7, L_f = 0.25, and $W \times H$ = 15 × 15 cm^2): (a) x = 7.5 cm, y is on the line of fin length ($\Delta\bar{\psi} = 2.3 \times 10^{-4}$, $\Delta\theta = 2.5 \times 10^{-2}$), (b) x = 4.6875 cm, y is on the line of fin length ($\Delta\bar{\psi} = 2.3 \times 10^{-4}$, $\Delta\theta = 2.5 \times 10^{-2}$), (c) x = 4.6875 cm, y is between the line of fin length ($\Delta\bar{\psi} = 2.3 \times 10^{-4}$, $\Delta\theta = 2.5 \times 10^{-2}$), and (d) x = 1.875 cm, y is between the line of fin length ($\Delta\bar{\psi} = 2.3 \times 10^{-4}$, $\Delta\theta = 2.5 \times 10^{-2}$).

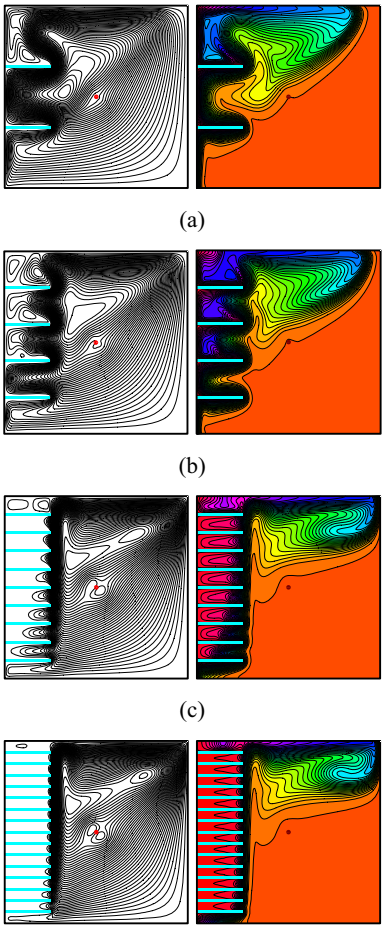

(a)

(b)

(c)

(d)

Fig. 5.24 Number of fins effect on the flow and temperature fields (V_0 = 12.0 kV, Ra = 10^6, N_e = 1, L_f = 0.25, and $W \times H$ = 15 × 15 cm^2): (a) N_f = 2 ($\Delta\bar{\psi}$ = 2.0 × 10^{-4}, $\Delta\theta$ = 2.5 × 10^{-2}), (b) N_f = 4 ($\Delta\bar{\psi}$ = 2.0 × 10^{-4}, $\Delta\theta$ = 2.5 × 10^{-2}), (c) N_f = 9 ($\Delta\bar{\psi}$ = 2.0 × 10^{-4}, $\Delta\theta$ = 2.5 × 10^{-2}), and (d) N_f = 15 ($\Delta\bar{\psi}$ = 2.0 × 10^{-4}, $\Delta\theta$ = 2.5 × 10^{-2}).

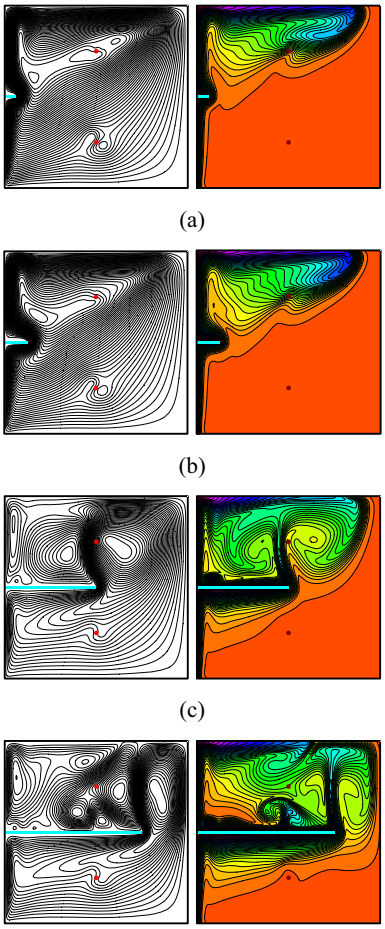

Fig. 5.25 Stream function and isotherm line contours inside the enclosures for various fin lengths (V_0 = 12.0 kV, Ra = 10^6, N_f = 1, N_e = 2, and $W \times H$ = 15 × 15 cm^2): (a) L_f = 0.0625 ($\Delta\bar{\psi} = 2.1 \times 10^{-4}$, $\Delta\theta = 2.5 \times 10^{-2}$), (b) L_f = 0.125 ($\Delta\bar{\psi} = 2.1 \times 10^{-4}$, $\Delta\theta = 2.5 \times 10^{-2}$), (c) L_f = 0.5 ($\Delta\bar{\psi} = 2.1 \times 10^{-4}$, $\Delta\theta = 2.5 \times 10^{-2}$), and (d) L_f = 0.75 ($\Delta\bar{\psi} = 2.1 \times 10^{-4}$, $\Delta\theta = 2.5 \times 10^{-2}$).

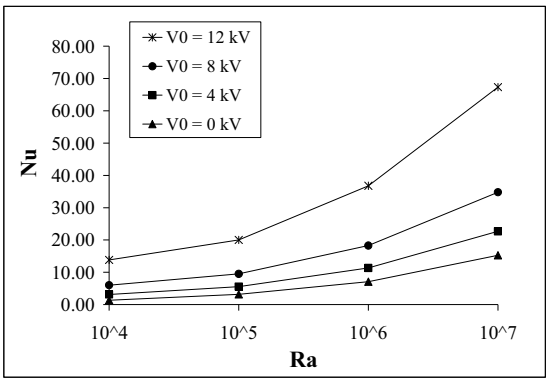

Fig. 5.26 Nusselt number as function of Rayleigh number (V_0 = 12.0 kV, N_f = 7, N_e = 1, L_f = 0.25, and $W \times H$ = 15 × 15 cm^2).

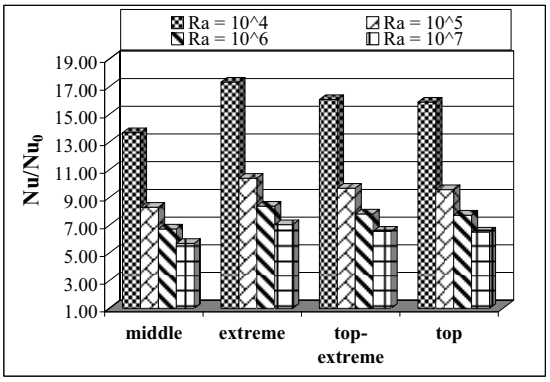

Fig. 5.27 Effect of the electrode arrangement on the heat transfer enhancement (V_0 = 12.0 kV, N_f = 7, N_e = 7, L_f = 0.25, and $W \times H$ = 15 × 15 cm^2).

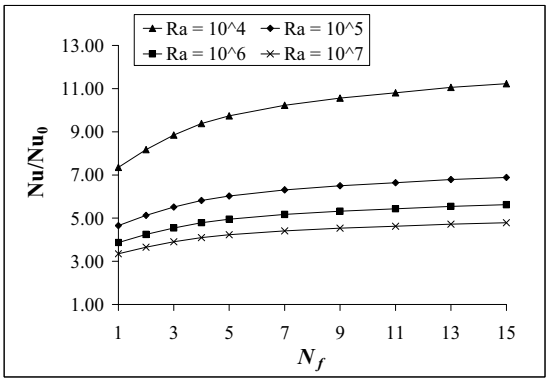

Fig. 5.28 Relation between the number of fins and augmented heat transfer (V_0 = 12.0 kV, N_e = 1, L_f = 0.25, and $W \times H$ = 15 × 15 cm^2).

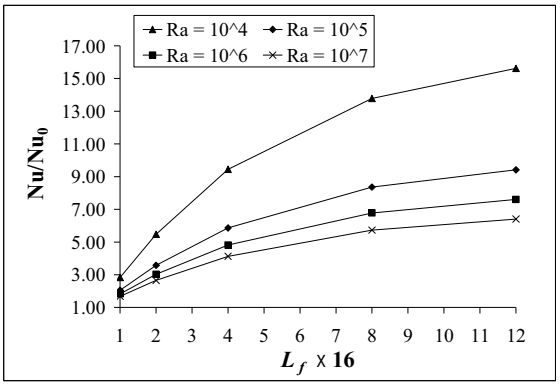

Fig. 5.29 Relation between the fin lengths and augmented heat transfer (V_0 = 12.0 kV, N_f = 1, N_e = 2, and $W \times H$ = 15 × 15 cm^2).

5.3 Open Vertical Channel Configuration

The computational domain and boundary conditions required for the governing equations are illustrated in Fig. 5.30. The left plate is maintained at uniform heat flux and the right plate is insulated, both upper and lower of channel are opening. All plates are electrically grounded and the channel size is 5 × 30 cm^2. Fig. 5.31 investigates the stream function contours of electrohydrodynamic applying while the Rayleigh number is varied between 10^4 - 10^7 in which an effect of Joule heating at the wire electrode is neglected (V_0 = 17.5 kV and N = 5). The flow patterns are oscillated due to the interaction between thermal buoyancy force and electrical body force. It can be observed that flow pattern in the channel is activated by an electric field at low Rayleigh number, but dominated by convective regime instead of an electric field as Rayleigh number increases further to 10^6 - 10^7 in Figs. 5.31(c)-(d). A convective regime is established at high Rayleigh number, the cold air is embarked through the bottom of opening, rises along the hot plate, and discharges at the top of opening. At low Rayleigh number, the temperature fields have been affected due to an electric field as represented in Fig. 5.32. It can be seen that temperature gradient (line density) at the left plate becomes higher with the increasing of Rayleigh number that cause high heat transfer coefficient develops along the hot plate.

The oscillatory stream function and isotherm line contours in categories of various numbers of electrodes from 5, 9, 17, and 33 are expressed in Figs. 5.33 and 5.34, respectively (V_0 = 17.5 kV and Ra = 10^6). The effect of number of electrodes plays much

important role on the air flow pattern in channel. It can be observed that the number of vortices increases when the number of electrodes is increased from 5 to 9 in Figs. 5.33(a)-(b), but the small vortices are combined and the large vortices occur at the upper and lower of the channel when the number of electrodes has sufficient excess at 17 to 33 in Figs. 5.33(c)-(d). The isotherm lines show formation of a boundary layer heat transfer along the hot plate in Fig. 5.34. As seen that temperature gradient at the left plate of Fig. 5.34(d) is highest compared with the other that obtains greatest heat transfer coefficient. Therefore, one can concluded that the effect of number of electrodes has more significant at a high value. Fig. 5.35 conducts the effect of electrode arrangements in bottom, top, ends, and middle denseness by exponential function while the number of electrodes is initially kept as the same at 17 (V_0 = 17.5 kV and Ra = 10^6). It is found that there are many vortices around the electrode strip especially at the high density zone and the flow patterns are oscillated due to the high intensity of an electric field. The temperature fields in channel are represented in Fig. 5.36. It can be seen that the large heat trap occurs in Fig. 5.39(b) due to the high flow resistant at the top of channel, while the other cases have uniform temperature gradient along the hot plate especially in Fig. 5.36(c) (ends denseness). This can be perceived that the temperature gradient, also convective heat transfer, should be highest in this case.

An augmented ratio of volume flow rate (per unit depth) inside channel is indicated Fig. 5.37 (V_0 = 17.5 kV). Fig. 5.37 shows a comparison of electrode arrangement effect to the augmented volume flow rate which found that bottom denseness performs highest performance. The reason of this result can be described by the fluid is rapidly conveyed by this arrangement along the hot plate from Fig. 5.36(a) that advantage for convective phenomenon. This is clearly seen from Fig. 5.38, number of electrode being the same, for which an optimum arrangement (bottom denseness) that ascertained from the predicted value of the flow arrangement in Fig. 5.37 has dramatically contrasted with this figure. The ends denseness (Fig. 5.36(c)) has more uniform distribution of temperature gradient in Fig. 5.36, which cause the maximum heat transfer enhancement (from the thinness thermal boundary layer) occurs approximately around 25% higher than in the case of non-EHD in Fig. 5.38.

Fig. 5.39 represents the relation between the heat transfer enhancement and channel aspect ratio (V_0 = 17.5 kV and W = 5 cm). In general, the augmented ratio decreases at high gap between wire and plate electrodes due to low intensity of an electric field. When a gap is initially fixed, the enhanced ratio reaches to the first maximum point at a rather low

number of electrodes and reduces slowly when the number is augmented. However, the enhanced ratio becomes increasingly again when the number of electrodes is sufficiently exceeded due to the high intensity of an electric field. The reason can be described by consider the value of ratio between distance between wire electrodes and distance between vertical plates, the maximum point occurs when this value immediately approach to 1 (or at $N = 1$ for $H = 10$ cm, $N = 5$ for $H = 30$ cm, and $N = 9$ for $H = 50$ cm). The electric field from each wire electrode emanates from a point charge symmetrically in all directions. Field lines begin on positive (wire electrode) and end on negative (grounded plate), they can not simply terminate in computational domain. At this electrode distance ratio, it may be advantage for polarization of ionic wind to the grounded plate. Thus, it can be noticed that the ratio of heat transfer enhancement increases in relation with the small gap and the suitable electrode distance ratio.

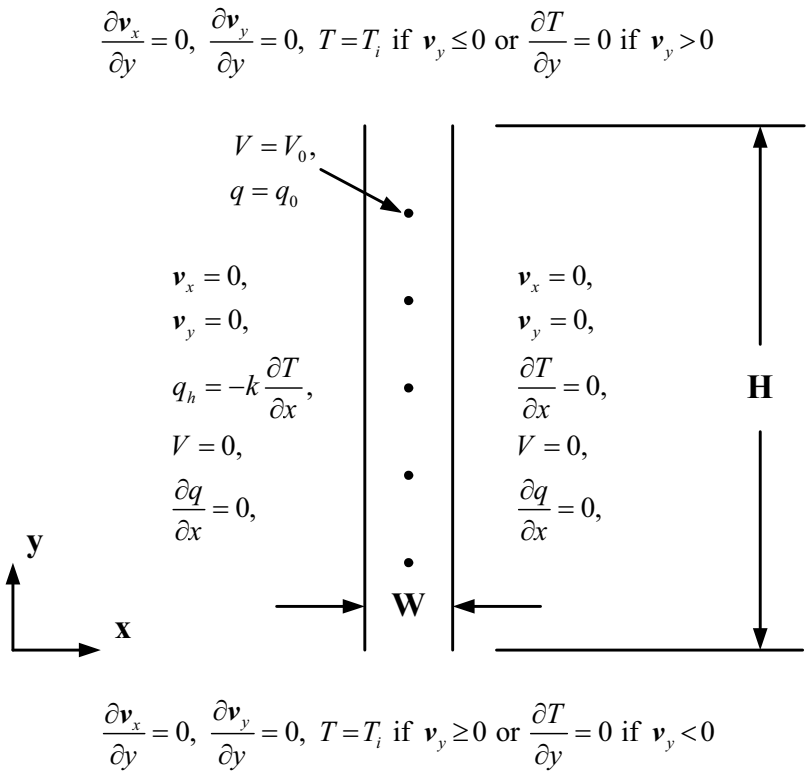

Fig. 5.30 Computational domain and boundary conditions.